

**Manuscript ID:** amt-2020-255

**Title:** An uncertainty-based protocol for the setup and measurement of soot/black carbon emissions from gas flares using sky-LOSA

**Authors:** Conrad, Bradley M.; Johnson, Matthew R.

### **Point-by-point Response to Comments by Referee #1**

*The manuscript amt-2020-255 by Conrad and Johnson describes a software heuristic for assisting a remote optical technique (skylight line-of-sight attenuation; skyLOSA) for measuring soot/black carbon emissions in large industrial flames. The technique allows a user to select the most reasonable position to set up the skyLOSA camera for a given set of flare and sky conditions. The computations behind this technique are intensive, so the manuscript spends some time describing a useful pre-computation approach. The pre-computed values are later used as inputs to a Monte Carlo uncertainty calculation.*

*From the skyLOSA perspective, the manuscript does not present new concepts or results. The main novel concept of this work is to apply the same theory used during detailed analysis to measurement, so that the measurement can be carefully configured to provide optimal results. This is a generally interesting concept, but could be considered as a technical note rather than a manuscript.*

*I recommend substantially shortening the manuscript's description of skyLOSA in order to reflect the subsequent conclusions. I also have reservations about the assumptions made in the MC analysis, especially the assumption that the flame emits only soot and no volatiles. These and other comments are detailed below.*

We thank the Referee for their review of this manuscript and have addressed their comments on a point-by-point basis below. While this manuscript does not present new sky-LOSA *field measurement data*, it does describe novel and significant improvements to the sky-LOSA technique. These noteworthy advancements enable both a thorough general uncertainty analysis and considerably accelerated post-processing of sky-LOSA data, as detailed in our responses below. Moreover, the new open-source software tool developed, tested, and released in conjunction with this manuscript, extends the presented general uncertainty analysis data and, for the first time, allows in-field estimates of uncertainty at the time of measurement, greatly simplifying the use of the sky-LOSA technique and opening it up to others.

Based on the Referee's feedback we have nevertheless made revisions to shorten the manuscript, while further strengthening the discussion and referencing. These include a reduction in the overall length by moving some details of the employed Monte Carlo (MC) method to a new appendix, Appendix A. While the validation of assumptions noted as technical concerns by the reviewer have been largely addressed in previous work, we have made these references clearer in the manuscript and have revised text where necessary to ensure the justification of assumptions in the present work is evident.

#### **General Comments:**

**Length.** *The manuscript often reads like a hybrid between a doctoral thesis and an instrument manual, especially in Sections 2, 3, 4.1.2, and 4.2. The text is well written, but inappropriately long. The audience here is not reading to reproduce skyLOSA calculations, but to understand the general concepts used. Please either cite other work or move this text to a supplement. This text can be replaced by short descriptions focussed on key concepts.*

The presented methodology – specifically the expansion of the scattering phase function, creation of sky categories/groups, and implementation of the variance-reducing MC method – is a novel and significant advancement to the sky-LOSA algorithm that was necessary to enable the presented general uncertainty analysis. Moreover, this new approach is now used in the post-processing phase of sky-LOSA to more-efficiently compute flare BC emissions from image data. Therefore, to explicitly justify necessary assumptions and to support others in the analysis of sky-LOSA data, we chose to describe the procedure in detail. However, we do agree that some of this theory can be placed in an appendix without sacrificing the readability of the manuscript and the understandability of the results and implications.

To reduce the length of the main manuscript, we have made the following revisions:

- Merged original Sections 3.1.1 and 3.1.2 into a single section (Section 3.1.1 in the revised document) that describes the Fourier-Legendre expansion of the scattering phase function (SPF) and provides the updated framework for computing skylight and sunlight inscattering.

- Moved original Section 3.1.3, describing how we model solar irradiance, into Appendix A (Section A.2).
- Moved original Section 3.1.4, describing the truncation of the Fourier-Legendre-expanded SPF, into Appendix A (Section A.1) – see also our response to the Referee’s last minor comment.
- Shortened original Section 3.2.1 and merged it with original Section 3.2 – see also our response to the Referee’s first minor comment.

We have also revised text in Section 3 to identify that the presented theory represents the current standard approach to analyzing sky-LOSA data; specifically, “[t]his section describes the MC method used in the present [general uncertainty analysis] including novel updates to the MC approach that are necessary to make this present work tractable and significantly accelerate future sky-LOSA analyses.”

**Length (continued).** *Similarly, too many acronyms are used in these sections and are not used frequently enough to be necessary (including ET, SPF, CM-LHS, ...) and not all symbols are defined next to their equations (e.g.  $L(b)$  in Equation 9 and  $ak$  next to Equation 18).*

We have deleted unnecessary acronyms in the manuscript and clarified symbols/nomenclature.

**Monte Carlo clarification.** *A Monte Carlo calculation randomly samples prior distribution(s) and repeats a calculation in order to obtain a posterior distribution of results. The key question here is what priors were assumed, and how accurate are they? The manuscript glosses over this point and takes the MC output as correct without any top-down validation. Please revise Section 3 and Table 2 to emphasize the prior distributions used. The authors have already done this in their earlier work (Johnson et al., 2013, Table 2) by tabulating "Distributions used in MC". I believe the authors did intend to include this information but I do not find it clear enough.*

Prior distributions for the eight fundamental soot properties required by the sky-LOSA method were derived from a thorough literature review of soot generated from flare-like flames. We originally referenced the source for these distributions (Johnson et al., 2013) but have now included them in the updated Table 2 for completeness. Further to the comments of Referee #3, we also now list the properties at the first mention of vector  $\mathbf{b}$  in Section 2.

**Monte Carlo clarification (continued).** *In Table 2 of this work, the last column "MC Implementation" is specified as "MC-randomized" multiple times – this is a meaningless statement. Of course the MC calculation performs random sampling.*

We have removed the term “MC- (Monte Carlo)-randomized” and instead refer to variables perturbed within MC analyses as *random* variables.

**Validation of assumptions.** *The manuscript assumes throughout that a perfect skyLOSA measurement gives a perfect result. This has not been justified in the manuscript nor in earlier skyLOSA work, to my knowledge. These calculations are not constrained by any direct measurements. The skyLOSA approach is comparable to a satellite retrieval algorithm and requires direct validation. Until directly validated, this limitation must always be repeated.*

In the case of sky-LOSA, there is no comparable quantitative reference standard for time-resolved soot/BC emissions from open flames like gas flares; the current measurement standard is an assessment of plume opacity by a human observer (U.S. EPA, 1974). However, significant validation work of the sky-LOSA approach and underlying assumptions has indeed been performed using a range of alternate approaches, as necessary.

The novel aspect of sky-LOSA is the quantification of soot/BC mass column density along a line-of-sight traversing a plume using radiometric observations coupled with radiative transfer considerations. As the enabling component of sky-LOSA, this theory (presented in Section 2 of the original manuscript) has been the focus of a range of validation efforts. As referenced in the first line of Section 2, the first-generation of the sky-LOSA approach was validated by Johnson et al. (2010) against a commercial laser-induced incandescence instrument and the proven lab-based diffuse-LOSA measurement (Thomson et al., 2008) on which the technique is ultimately based. Proof-of-concept field measurements were subsequently performed in Uzbekistan (Johnson et al., 2011). Johnson et al., (2013) then extended the earliest theory to consider the effect of inscattering of skylight and sunlight that bias the perceived opacity of the plume and, hence, emission rate. In this same work, they derived the prior distributions of soot/BC properties used in the present sky-LOSA method to bound the

influence of uncertain soot/BC properties on computed emissions. This theory was used in field measurements in Mexico and Ecuador (Conrad and Johnson, 2017; Johnson et al., 2013).

At this point, sky-LOSA had been validated in its ability to quantify soot/BC mass loading and the theory developed to robustly consider uncertain soot/BC properties and inscattering effects. Validation efforts then turned to two final radiative transfer considerations that could influence sky-LOSA's ability to accurately quantify soot/BC loading. Conrad et al. (2020a) leveraged large-eddy simulations of flares to prove that the effect of refractive index gradient-driven beam steering in flare plumes was negligible in the visible spectrum where sky-LOSA data are acquired. Then, Conrad et al. (2020b) amended the sky-LOSA theory to consider the minor/second-order effect of multiple scattering on the quantification of inscattered light in sky-LOSA analyses. From the perspective of first principles, these analyses completed our efforts to validate the sky-LOSA technique.

To direct the interested reader to these substantial validation efforts, we have revised the first line of Section 2 to reference validation-related publications.

***Validation of assumptions (continued).*** *The concentrations reported by the current approach are a type of "equivalent black carbon" defined by the authors' assumptions.*

As discussed in the seminal works of Andreae and Gelencsér (2006) and Petzold et al. (2013), light absorption measurements of "black carbon" mass are inherently defined by the assumed optical properties of the absorbing particulate. These manuscripts both suggest use of the term "equivalent black carbon" for absorption-based techniques although this term has not been broadly adopted within the literature. Instead, it is generally implied that BC measured using such optical techniques is inherently "equivalent BC".

Thus, we absolutely agree with the Referee and have revised the text in Section 2 to specifically note that sky-LOSA-reported mass emissions are dependent upon the prior soot/BC property distributions:

*"..., it is worth noting that these prior distributions of soot/BC properties inherently link light absorption measurements and computed mass column density/emissions using sky-LOSA. Thus, in keeping with Andreae and Gelencsér (2006) and Petzold et al., (2013), sky-LOSA-inferred soot/BC mass might be called 'equivalent BC' as is recommended for all light absorption-based diagnostics."*

***Validation of assumptions (continued).*** *My main concern here is with respect to the aerosol optical properties, which have not been discussed at all. Instead, Johnson et al. 2013 is cited. The authors have assumed that the flame emits only soot. What about organics, which may condense when the plume cools? The photograph in Johnson et al. 2013 clearly suggests that the plume may have cooled before measurement. What about inorganics such as sulfates? How pure are the fuels burnt in these flares? Any impurities are likely to influence the aerosol optical properties. Please add calculations where black carbon is assumed to be mixed with organics or other impurities, using reasonable and literature-based assumptions, and show how the conclusions of this work change in response.*

The Referee's main concern is that the presence of non-BC material in flare plumes could bias sky-LOSA-computed soot/BC emissions by their influence on aerosol optical properties. While this is somewhat at odds with the notion of "equivalent BC" (see the Referee's previous comment) – i.e., inferred mass is *operationally defined* by the assumed optical properties – numerous observations in the literature show that non-BC material does not contribute to optical observations of fresh flare plumes in the visible spectrum.

In theory, both internal and external mixtures of soot/BC with other material could bias sky-LOSA-calculated emissions by changing the optical properties of particulate in the flare plume:

1. If emitted soot/BC were internally mixed/coated with a scattering material (via condensation of co-emitted organic species, for example), then emitted BC could have enhanced absorption (e.g., Bond et al., 2006).
2. Alternatively, if emitted soot/BC were externally mixed with significant co-emitted primary (and secondary) aerosols, the effective absorption/scattering by the plume could be different than that of soot/BC alone.

For the specific case of gas flares, it has been observed both in the laboratory and the field that optically active material in the visible spectrum in flare plumes is solely soot/BC. First, in their field measurements in the Bakken region, Schwarz et

al., (2015) showed that “flaring BC was not associated with optically significant internally mixed non-BC material or with significant emissions of non-BC-containing primary aerosol”. Similarly, Weyant et al., (2016) concluded in their field measurements that the presence of non-BC aerosols in a flare plume is “not statistically different from zero”. Importantly, sky-LOSA measurements are performed in the very near-field of the flame – e.g., the noted Fig. 2 in Johnson et al. (2013) shows sky-LOSA measurement of emissions over a control surface that is within meters of the flame tip. While the plume has indeed cooled at this location (likely within 200 K of ambient temperature (Poudenx, 2000)), the soot/BC particulate is very fresh relative to typical atmospheric soot/BC that may be internally mixed with other materials. In fact, the aforementioned field studies were performed well downstream of the flame (at the basin level in the case of Schwarz et al., (2015) and hundreds of meters downstream in the case of Weyant et al., (2016)), where particles would have been subject to much more atmospheric aging and thus much more likely to be mixed with non-BC material.

These field observations are supported by laboratory studies of freshly emitted soot/BC from large flare-like flames burning fuels representative of global oil and gas flaring. Specifically, electron micrographs from Kazemimanesh et al. (2019) identify that co-emitted organics are not present as a coating on flare-emitted soot/BC. This is likely because emitted organics are largely unburned fuel (Johnson et al., 2001) which are dominated by highly volatile, low molecular weight hydrocarbons (e.g., Conrad and Johnson, 2019).

Thus, these literature data conclusively show that fresh flare particulate as measured by sky-LOSA is soot/BC, which supports our use of the literature-derived flare soot/BC properties from Johnson et al. (2013).

**Validation of assumptions (continued).** *A lesser concern is the assumption (Section 3.1.3) of an ideal clean atmosphere. What about background aerosol? Surely the air around an oil field is not perfectly clean.*

The sky-LOSA method does not inherently assume an ideal clean atmosphere. The original Section 3.1.3 (now Appendix Section A.2) discussed how we model ground-level solar irradiance in the context of the sky-LOSA Monte Carlo method. We believe that the Referee is referring to the “ideal extinction for a clean atmosphere at a given relative air mass” ( $\sigma^{e*}(m)$ ) that is used to compute the ground-level solar irradiance from the extra-terrestrial solar irradiance. Importantly, this ideal extinction is multiplied by the sky-dependent turbidity factor ( $T(a)$ ) to represent extinction through a non-ideal (i.e., polluted) atmosphere. That is, an ideal clean atmosphere is **not** assumed, but is scaled to represent a range of realistic atmospheric conditions. To clarify this in the revised manuscript, we have included the new text (in bold):

“... $\sigma^{e*}$  is the ideal extinction for a clean atmosphere at a given relative air mass, and  $T(a)$  is the model-dependent turbidity factor **that is used to consider realistic atmospheres and describes the number of clean atmospheres required to represent **attenuation through the non-ideal, polluted atmosphere.****”

#### **Minor Comments:**

*The justification of a quantile-based coefficient of variation in Section 3.2.1 can be shortened.*

We have shortened this section as requested and merged it into the preceding section, 3.2.

*The word compiled in Section 3.1.5 should probably be changed to grouped. And I am not sure I understand what concept the authors are trying to convey here. Was the grouping done based on skyLOSA results?*

We have removed the word “compiled” and amended our original notation to say “sorted into sky ‘categories’”.

In our original text, we present the concept (emphasis added) that “...there is some additional uncertainty in sky-LOSA-computed soot mass column density through use of a **single** CIE sky model in the MC method” due to the inherent error in these simple models. We also present how the sky categories were defined (emphasis added): “...to permit capture of CIE sky model error in the [general uncertainty analysis], like skies were [sorted] into sky ‘[categories]’ **that have similar properties but differing ... directional variability.**” Broad descriptions and characteristics of each sky category are located in the final paragraph of Section 3.1.2 and Table 1 of the revised manuscript.

*I found the discussion of the total order  $L(b)$  in Section 3.1.4 unclear. Is this discussion significant, considering the uncertainties in the assumption of a black-carbon-only aerosol and aerosol-free sky?*

As noted in the responses above, we do not assume an aerosol-free sky.

This brief section describes our approach to the truncation of the Fourier-Legendre expansion of the scattering phase function; specifically, the order ( $L(\mathbf{b})$ ) at which the expansion was truncated while both ensuring accuracy in sky-LOSA-computed soot/BC mass column density and enabling rapid calculation of sky- and sunlight inscattering. To help reduce the length of the main manuscript (see the Referee’s first general comment), we have moved this text to the new Appendix A (Section A.1).

### **Point-by-point Response to Comments by Referee #3**

*This manuscript presented an uncertainty-based guide/instruction for potential users of the sky-LOSA technique to measure soot/black carbon emissions from flares in the oil and gas industry. Although the method itself and the details of various models involved in the data analysis have been published by the authors, the paper is useful to help potential researchers/engineers to better understand and apply this promising technique. The paper is well written as deserves publication. I have few questions/comments for the authors to consider.*

We thank the Referee for their positive comments and recognition of the value of the manuscript and software tool to help others to “better understand and apply this promising technique”.

1. *In line 29 on page 4, please explicitly list the eight soot properties.*

We have appended a list of these eight soot properties to the noted paragraph. Further to the comments of Referee #1, we have also included the properties and their distributions in Table 2 of the revised manuscript.

2. *In the derivation of Eq. (4), do you need to assume that the mass-normalized extinction cross section of soot is constant everywhere in the flare? Otherwise, it cannot be taken out of the second integral on the right-hand side of Eq. (4).*

To remove the mass-normalized extinction cross-section from this integral we must assume that it does not vary in space. This assumption is supported by spatially resolved measurements of soot properties within the literature. For example, Köylü and Faeth's (1992) measurements of soot morphology in the overfire region of large-scale buoyancy-driven turbulent diffusion flames have shown that “the structure of soot ... is relatively independent of ... position in the overfire region” – and stated more conclusively in a later publication (1994): “...soot structure is independent of position in the overfire region...”. We have clarified this assumption in Section 2 of the revised manuscript.

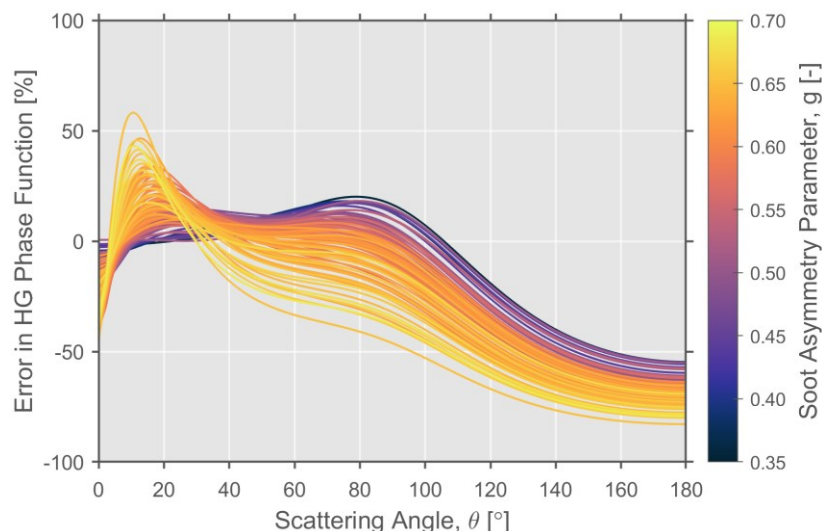
Although we inherently assume spatiotemporal uniformity of the soot properties, it is important to note that these soot properties are independently perturbed within sky-LOSA’s Monte Carlo analysis to bound the influence of their uncertainty on sky-LOSA-computed emissions.

3. *In this work, the authors dealt with the in-scattering term by expanding the SPF in Fourier-Legendre series. As the authors admitted, this expansion requires a large number of terms to have an accurate representation of the SPF, especially when it is highly forward peaked. There are other methods to more efficiently deal with highly-forward peaked SPF, such as the Henyey-Greenstein and transport approximations, have the authors considered such approaches in the calculations of the in-scattering terms?*

Although there are a few different options for modelling scattering phase functions (SPFs), the Fourier-Legendre expansion has the advantage of being numerically exact, even if more computationally demanding. Moreover, while not as efficient as the HG phase function, calculation of the Legendre coefficients was quite rapid when following the approach of Schuster (2004) such that their computation was negligible compared to the execution of the Monte Carlo method of the present general uncertainty analysis.

Early in this research we did consider the Henyey-Greenstein (HG) phase function as suggested by the reviewer, but ultimately decided that it was not suitable for the sky-LOSA technique. To elaborate, the HG phase function is a simple one-parameter model that approximates the soot/Legendre coefficients via  $\Phi_l = g_{HG}^l (2l + 1)$  (e.g., Boucher, 1998), where  $g_{HG}$  is the “anisotropy factor” of the phase function that is usually estimated via least-squares fitting to the RDG-computed SPF (e.g., Daun et al., 2008). While the HG phase function renders calculation of the soot coefficients trivial, our experience has shown that the single-parameter HG phase function may not always capture the highly asymmetric SPFs that are typical of soot, especially larger aggregate populations. The below figure plots the angle-resolved error of the HG phase function for a range of soot properties obtained using the prior distributions in the manuscript – here, the colour of each plot represents the asymmetry parameter of the soot population. The figure shows that errors can exceed 50% but, more

importantly and perhaps unsurprisingly, these errors tend to be highest for large aggregates where the SPF is more asymmetric. This implies that the HG phase function is a poorer alternative in the context of sky-LOSA, where measurement uncertainty is largely controlled by the forward scattering of sky- and sunlight into the camera (as discussed in the text surrounding Fig. 4 in the original manuscript).



4. In this paper, the authors did not provide the detailed soot properties, but reference to a previous study. It appears that the authors assume that the soot properties are uniform over the entire flare under consideration and also remain the same from one flare to another. Is this correct? If yes, the authors need to justify this assumption. The soot properties in a flare with soot emission reduction measure (such as partial premixing) may not be the same as those without any such measures.

While we defensibly assume spatiotemporal uniformity of soot properties *within a given draw* of the Monte Carlo (MC) analysis (see the Referee’s second comment), it is important to note that these soot properties are perturbed within the MC method over notably broad prior distributions. These prior distributions were derived from an exhaustive literature review of soot property data (Johnson et al., 2013), including studies of soot generated by flames of varying scales and configurations (premixed/non-premixed) burning fuels that extend well beyond typical flare gas compositions. Despite the likely variability of soot properties from flare to flare, the breadth of these priors suggests that sky-LOSA confidence intervals are likely to bound the ground truth emission rate; for this reason, the same prior distributions of soot properties are used in all sky-LOSA analyses.

5. The choice of sky model group seems not straightforward and has a strong influence on the measurement. I wonder if the authors can provide more useful ‘tips’ to make such a choice for new users of sky-LOSA.

Sky categories/groups are selected using criteria laid out in the rightmost column of Table 1. These criteria are based on simple observations by the sky-LOSA user such as whether the sun is obstructed or unobstructed and whether the sky is overcast, partly cloudy, or clear. Sky-LOSA-calculated soot emissions are indeed sensitive to the selected CIE sky model; however, *within* each of the defined sky categories/groups (e.g., highly turbid overcast skies (category/group “A”)), different sky models generally have similar effects on computed emissions and uncertainties. In fact, it is this weak variation in the effect of the models within a sky category/group that allows us to define the sky categories/groups and ultimately treat the sky model as a random parameter within the MC analysis with minor impact on measurement uncertainty.

To clarify how a user might select the most appropriate sky category/group, we have added text to Section 3.1.2 of the revised manuscript noting the simple selection criteria.

## **References**

- Andreae, M. O. and Gelencsér, A.: Black carbon or brown carbon? The nature of light-absorbing carbonaceous aerosols, *Atmos. Chem. Phys.*, 6(10), 3131–3148, doi:10.5194/acp-6-3131-2006, 2006.
- Bond, T. C., Habib, G. and Bergstrom, R. W.: Limitations in the enhancement of visible light absorption due to mixing state,

- J. Geophys. Res., 111(D20), D20211, doi:10.1029/2006JD007315, 2006.
- Boucher, O.: On Aerosol Direct Shortwave Forcing and the Henyey–Greenstein Phase Function, *J. Atmos. Sci.*, 55(1), 128–134, doi:10.1175/1520-0469(1998)055<0128:OADSFA>2.0.CO;2, 1998.
- Conrad, B. M. and Johnson, M. R.: Field measurements of black carbon yields from gas flaring, *Environ. Sci. Technol.*, 51(3), 1893–1900, doi:10.1021/acs.est.6b03690, 2017.
- Conrad, B. M. and Johnson, M. R.: Mass absorption cross-section of flare-generated black carbon: Variability, predictive model, and implications, *Carbon N. Y.*, 149, 760–771, doi:10.1016/j.carbon.2019.04.086, 2019.
- Conrad, B. M., Thornock, J. N. and Johnson, M. R.: Beam steering effects on remote optical measurements of pollutant emissions in heated plumes and flares, *J. Quant. Spectrosc. Radiat. Transf.*, 254, doi:10.1016/j.jqsrt.2020.107191, 2020a.
- Conrad, B. M., Thornock, J. N. and Johnson, M. R.: The effect of multiple scattering on optical measurement of soot emissions in atmospheric plumes, *J. Quant. Spectrosc. Radiat. Transf.*, 254, 107220, doi:10.1016/j.jqsrt.2020.107220, 2020b.
- Daun, K. J., Thomson, K. A. and Liu, F.: Simulation of Laser-Induced Incandescence Measurements in an Anisotropically Scattering Aerosol Through Backward Monte Carlo, *J. Heat Transfer*, 130(11), 1–10, doi:10.1115/1.2955468, 2008.
- Johnson, M. R., Wilson, D. J. and Kostiuk, L. W.: A fuel stripping mechanism for wake-stabilized jet diffusion flames in crossflow, *Combust. Sci. Technol.*, 169(1), 155–174, doi:10.1080/00102200108907844, 2001.
- Johnson, M. R., Devillers, R. W., Yang, C. and Thomson, K. A.: Sky-Scattered solar radiation based plume transmissivity measurement to quantify soot emissions from flares, *Environ. Sci. Technol.*, 44(21), 8196–8202, doi:10.1021/es1024838, 2010.
- Johnson, M. R., Devillers, R. W. and Thomson, K. A.: Quantitative field measurement of soot emission from a large gas flare using sky-LOSA, *Environ. Sci. Technol.*, 45(1), 345–350, doi:10.1021/es102230y, 2011.
- Johnson, M. R., Devillers, R. W. and Thomson, K. A.: A generalized sky-LOSA method to quantify soot/black carbon emission rates in atmospheric plumes of gas flares, *Aerosol Sci. Technol.*, 47(9), 1017–1029, doi:10.1080/02786826.2013.809401, 2013.
- Kazemimanesh, M., Dastanpour, R., Baldelli, A., Moallemi, A., Thomson, K. A., Jefferson, M. A., Johnson, M. R., Rogak, S. N. and Olfert, J. S.: Size, effective density, morphology, and nano-structure of soot particles generated from buoyant turbulent diffusion flames, *J. Aerosol Sci.*, 132, 22–31, doi:10.1016/j.jaerosci.2019.03.005, 2019.
- Köylü, Ü. Ö. and Faeth, G. M.: Structure of overfire soot in buoyant turbulent diffusion flames at long residence times, *Combust. Flame*, 89(2), 140–156, doi:10.1016/0010-2180(92)90024-J, 1992.
- Köylü, Ü. Ö. and Faeth, G. M.: Optical properties of overfire soot in buoyant turbulent diffusion flames at long residence times, *J. Heat Transfer*, 116(1), 152–159, doi:10.1115/1.2910849, 1994.
- Petzold, A., Ogren, J. A., Fiebig, M., Laj, P., Li, S.-M., Baltensperger, U., Holzer-Popp, T., Kinne, S., Pappalardo, G., Sugimoto, N., Wehrli, C., Wiedensohler, A. and Zhang, X.-Y.: Recommendations for reporting “black carbon” measurements, *Atmos. Chem. Phys.*, 13(16), 8365–8379, doi:10.5194/acp-13-8365-2013, 2013.
- Poudenx, P.: Plume sampling of a flare in crosswind: structure and combustion efficiency, M.Sc. Thesis, University of Alberta, Edmonton, AB, Canada, Edmonton. [online] Available from: [http://www.collectionscanada.gc.ca/obj/s4/f2/dsk1/tape4/PQDD\\_0011/MQ59867.pdf](http://www.collectionscanada.gc.ca/obj/s4/f2/dsk1/tape4/PQDD_0011/MQ59867.pdf), 2000.
- Schuster, G. L.: Inferring the Specific Absorption and Concentration of Black Carbon From Aeronet Aerosol Retrievals, Pennsylvania State University., 2004.
- Schwarz, J. P., Holloway, J. S., Katich, J. M., McKeen, S., Kort, E. A., Smith, M. L., Ryerson, T. B., Sweeney, C. and Peischl, J.: Black carbon emissions from the Bakken oil and gas development region, *Environ. Sci. Technol. Lett.*, 2(10), 281–285, doi:10.1021/acs.estlett.5b00225, 2015.
- Thomson, K. A., Johnson, M. R., Snelling, D. R. and Smallwood, G. J.: Diffuse-light two-dimensional line-of-sight attenuation for soot concentration measurements, *Appl. Opt.*, 47(5), 694–703, doi:10.1364/AO.47.000694, 2008.
- U.S. EPA: Visual Determination of the Opacity of Emissions from Stationary Sources, Code of Federal Regulations, Title 40, Part 60, Appendix A-4, Method 9, United States of America., 1974.

Weyant, C. L., Shepson, P. B., Subramanian, R., Cambaliza, M. O. L. L., Heimburger, A., McCabe, D., Baum, E., Stirm, B. H. and Bond, T. C.: Black carbon emissions from associated natural gas flaring, *Environ. Sci. Technol.*, 50(4), 2075–2081, doi:10.1021/acs.est.5b04712, 2016.



# An uncertainty-based protocol for the setup and measurement of soot/black carbon emissions from gas flares using sky-LOSA

Bradley M. Conrad, Matthew R. Johnson

Energy and Emissions Research Laboratory, Department of Mechanical and Aerospace Engineering, Carleton University,  
Ottawa, ON K1S 5B6, Canada

Correspondence to: Matthew R. Johnson ([matthew.johnson@carleton.ca](mailto:matthew.johnson@carleton.ca))

**Abstract.** Gas flaring is an important source of atmospheric soot/black carbon, especially in sensitive Arctic regions. However, emissions have traditionally been challenging to measure and remain poorly characterized, confounding international reporting requirements and adding uncertainty to climate models. The sky-LOSA optical measurement technique has emerged as a powerful means to quantify flare black carbon emissions in the field, but broader adoption has been hampered by the complexity of its deployment, where decisions during setup in the field can have profound, non-linear impacts on achievable measurement uncertainties. To address this challenge, this paper presents a prescriptive measurement protocol and associated open-source software tool that simplifies acquisition of sky-LOSA data in the field. Leveraging a comprehensive Monte Carlo-based General Uncertainty Analysis (GUA) to predict measurement uncertainties over the entire breadth of possible measurement conditions, general heuristics are identified to guide a sky-LOSA user toward optimal data collection. These are further extended in the open-source software utility, *SetupSkyLOSA*, which interprets the GUA results to provide detailed guidance for any specific combination of location, date/time, and flare, plume, and ambient conditions. Finally, a case study of a sky-LOSA measurement at an oil and gas facility in Mexico is used to demonstrate the utility of the software tool, where potentially small region(s) of optimal instrument setup are easily and quickly identified. It is hoped that this work will help increase the accessibility of the sky-LOSA technique and ultimately the availability of field measurement data for flare black carbon emissions.

## 1 Introduction

Gas flaring is a routine practice in the oil and gas industry in which producers and refiners burn excess or unwanted gases in open-atmosphere flames, typically from vertical pipe stacks. Flaring is generally preferable to the venting of gases to atmosphere because it reduces carbon dioxide (CO<sub>2</sub>)-equivalent emissions; however, flaring still emits potent climate-forcing pollutants directly to atmosphere (Allen and Torres, 2011; Johnson et al., 2001, 2011, 2013; McDaniel, 1983; Pohl et al., 1986). These pollutants have public health implications (e.g., Anenberg et al., 2012) and include unburnt hydrocarbons, volatile organic compounds, and particulate matter (U.S. EPA, 2018). Soot particulate matter (commonly referred to as black carbon, BC) has been suggested by some to be the second-most potent climate forcer after CO<sub>2</sub> (Bond et al., 2013; Jacobson,

2001; Ramanathan and Carmichael, 2008; Sato et al., 2003). Annual flaring is estimated by satellite imagery to be ~140 billion m<sup>3</sup> (Elvidge et al., 2007, 2009, 2016), making it one important source of global soot emissions. Although other industrial sectors dominate gas flaring in absolute soot emissions, the locations of flaring activities (particularly in Russia) likely have a disproportionate impact on the sensitive arctic climate due to efficient transport pathways penetrating the arctic air mass (e.g., Popovicheva et al., 2017; Stohl et al., 2006).

With the addition of BC to the Gothenburg protocol in 2012 (United Nations Economic Commission for Europe (UNECE), 2012), 34 countries are now legally bound to report, where data are available, soot/BC emissions under UNECE's Convention on Long-Range Transboundary Air Pollution, including the European Union, Russia, United States of America, and Canada. To attribute – and, hence, report and regulate – soot/BC emissions from various sources, emission factors that relate soot/BC emissions to a measure of industrial activity are required. Unfortunately, for gas flaring, commonly employed soot emission factors are crude single-valued parameters that link emitted soot mass to volume/mass of gas flared regardless of flare design, gas composition, or operating conditions. This contrasts with numerous studies that have observed a significant influence of flare gas composition and flame aerodynamics on soot emissions (Becker and Liang, 1982; Conrad and Johnson, 2017; McEwen and Johnson, 2012) and even soot properties (Conrad and Johnson, 2019; Trivanovic et al., 2020). Further soot yield data are needed, particularly for real-world flares under field conditions, to develop and validate accurate flare soot/BC emission factor models.

At present, there are only two published methods for the quantitative measurement of soot/BC emissions from individual in-field flares. One technique employs aircraft-based sampling of a flare plume (Gvakharia et al., 2017; Weyant et al., 2016), where measurements of soot, methane, and CO<sub>2</sub> concentrations during transects through the plume are used to provide flare-specific estimates of soot yield, using assumed flare gas compositions. The second technique is a ground-based remote optical measurement called sky-LOSA (line-of-sight attenuation using skylight; Conrad and Johnson, 2017; Johnson et al., 2010, 2011, 2013). Sky-LOSA quantifies time-resolved soot mass emission rates through analysis of highspeed image data. Parallel access to flare infrastructure permits simultaneous measurement of flare gas flow rate and gas sample extraction for off-site compositional analysis, which enables the *direct* calculation of soot yield for a targeted flare. To date, sky-LOSA has been deployed on 11 field measurement campaigns in Uzbekistan, Mexico, Ecuador, and Canada, providing 28 measurements of soot emissions from 17 unique flares (Conrad and Johnson, 2017; Johnson et al., 2011, 2013).

The key component of a sky-LOSA measurement is the quantification of plume soot loading using image data, via analysis and modelling of radiative transfer through the atmospheric flare plume at the measurement wavelength. For each acquired image, soot mass column density is resolved pixel-by-pixel over a control surface within the image plane to permit mass emission rate calculation. Uncertainties in sky-LOSA-calculated emission rate are computed under a Monte Carlo (MC) framework and are dominated by uncertainties that affect computation of soot mass column density. While these uncertainties are influenced by numerous parameters considered within the MC analysis, they are also sensitive to the positioning and pointing of the sky-LOSA camera relative to the horizon and sun. Consequently, a sky-LOSA user must position the camera according to several constraints, which may be heuristic but can also vary with uncontrollable measurement parameters. To

make the measurement technique accessible to end-users, enabling an increase in flare soot emissions data, a standardized data acquisition protocol for sky-LOSA is required.

The objective of this work is to complete a general uncertainty analysis (GUA) for the sky-LOSA measurement technique that provides uncertainty-based guidance to an end-user regarding the setup of equipment and acquisition of sky-LOSA data through an accompanying open-source software tool. A summary of sky-LOSA theory, referring to derivations in previous works, is first provided in Section 2 of this manuscript. The GUA methodology is summarized in section 3, including special provisions necessary to reduce the computational burden of the MC-based approach (section 3.1 and Appendix A). Representative results from the MC GUA are shown in section 4.1 and general heuristics for the acquisition of sky-LOSA data, including new observations based on MC GUA results are summarized in sections 4.1.1 and 4.1.2. To provide case-by-case guidance, a new open-source software tool to calculate sky-LOSA measurement uncertainty is introduced in section 4.2. Finally, in section 4.3, the software tool is used in a case study that analyses optimal camera positioning for flare measurements at a gas refining and transport facility in Campeche, Mexico. This work enables a consistent approach for the selection of sky-LOSA camera positioning and pointing to minimize measurement uncertainties, ultimately contributing to the standardization of the sky-LOSA measurement technique.

## 2 Sky-LOSA measurement

The generalized sky-LOSA theory was summarized in full by Johnson et al. (2013) and has been the subject of a variety of validation efforts (Conrad et al., 2020a, 2020b; Johnson et al., 2010). Development of the theory begins with Fig. 1, which shows an example sky-LOSA image for computation of time-resolved soot emission rate from a soot-laden flare plume in the Montney formation of Alberta, Canada. A highly linear, grayscale, scientific-CMOS camera (e.g., pco edge 5.5) is used to obtain upwards of ten minutes of high-speed image data of the flare and turbulent, soot-laden, atmospheric plume. Pseudo 16-bit images are acquired at framerates of 25–50 Hz with a narrow mid-visible bandpass filter ( $531 \pm 20$  nm) to yield a scene of spectrally integrated light intensity.

Overlaid in Fig. 1 is an example control surface ( $C$ ) of specified radius ( $r$  [m]), through which the instantaneous mass emission rate of soot ( $\dot{m}_s$  [ $\text{g s}^{-1}$ ]) may be computed. For an arbitrary control surface in three dimensions, the instantaneous mass flux of soot through the surface is:

$$\dot{m}_s = \iint_A (\rho_s \mathbf{u}) \cdot \mathbf{n} dA \quad (1)$$

where  $\rho_s$  is the mass concentration of soot [ $\text{g m}^{-3}$ ],  $\mathbf{u}$  is the local plume velocity vector [ $\text{m s}^{-1}$ ],  $\mathbf{n}$  is the unit vector locally normal to the control surface [–], and  $dA$  is an infinitesimal area [ $\text{m}^2$ ]. For sky-LOSA, where three-dimensional data along a pixel’s line-of-sight (LOS) are collapsed to two-dimensions through projection, an equivalent formulation for the instantaneous mass emission rate is:

**Deleted:** first validated by Johnson et al., (2010) and is summarized in full by Johnson et al. (2013)

$$\dot{m}_s = \int_C \rho'_s(r, \phi) u_n(r, \phi) r d\phi \quad (2)$$

where  $\rho'_s(r, \phi) = \int \rho_s(r, \phi, x) dx$  is the soot mass column density along a LOS (where the  $x$ -dimension is orthogonal to the image plane) [ $\text{g m}^{-2}$ ] and  $u_n(r, \phi) = (\int \rho_s(r, \phi, x) \mathbf{u}(r, \phi, x) \cdot \mathbf{n}(\phi) dx / \rho'_s(r, \phi))$  represents the component of the mass concentration-weighted, LOS-averaged, velocity of the plume [ $\text{m s}^{-1}$ ] that is normal to the control surface from the camera's perspective (as shown in the figure). Via Eq. (2), sky-LOSA thus requires knowledge of three items to compute the emission rate: spatial scaling of the image plane to accurately quantify  $r$ , the velocity field of the plume within the image plane (yielding  $u_n(r, \phi)$ ), and the soot mass column density resolved over the control surface. Spatial scaling of the image is obtained through use of a pinhole analogy for the sky-LOSA optics, coupled with a measurement of the distance to the flare stack tip by laser rangefinder (e.g., Laser Technology Inc. TruPulse 360R) (Johnson et al., 2013). Given that imaging is performed with a global shutter and at a sufficiently rapid framerate and exposure, the two-dimensional plume velocity field over the image plane is estimated via image correlation/particle image velocimetry, using a third party software suite such as LaVision DaVis 8.4 that includes a means of uncertainty quantification (Wieneke, 2015). Finally, the novel enabling aspect of sky-LOSA is the use of bounded knowledge of soot optical properties from literature data to compute the soot mass column density with accurate uncertainties via radiometric observations and modelling of radiative transfer within the atmosphere and plume. Example sky-LOSA-measurements of time-resolved soot emission rate are available in previous works (Conrad and Johnson, 2017; Johnson et al., 2011, 2013).

Figure 2 shows an example positioning/pointing of the sky-LOSA camera and an optical axis/LOS within the surrounding skydome. For a given LOS, a cartesian coordinate system is defined where the positive  $x$ -direction is the path that light travels into the camera, the positive  $z$ -direction is the general direction of plume motion, and the  $y$ -dimension completes the orthogonal system. To model radiative transfer, there are three boundary conditions that must be considered. Firstly, the ground is treated as a cold, black surface and is thus ignored within the sky-LOSA algorithm. Secondly, the sky is modelled as a diffuse, polarized source concomitant with atmospheric scattering of solar radiation. The distribution of skylight intensity ( $I(\alpha, \alpha_s, Z, Z_s, \alpha)$  [ $\text{W m}^{-2} \text{sr}^{-1}$ ]) and the incident intensity along the LOS ( $I^o(\alpha_s, \beta, Z_s, a)$  [ $\text{W m}^{-2} \text{sr}^{-1}$ ]) are considered using the standard models of the Commission Internationale de l'Eclairage (CIE, 2003), where the index  $a \in \{1 \dots 15\}$  indicates a specific CIE sky "type". Finally, ground-level normal solar irradiance ( $E_{sn}$  [ $\text{W m}^{-2}$ ]) is estimated using in-field, image-based measurements of the sun (Johnson et al., 2013) or modelled using the CIE models. With this radiative transfer model, sky-LOSA-quantification of soot mass column density proceeds with the radiative transfer equation (RTE):

$$I^t = I^o \exp\left(-\sigma_m^e(\mathbf{b}) \int_{-\infty}^L \rho_s(x) dx\right) + \int_{-\infty}^L J^s(x, \mathbf{b}) \rho_s(x) \exp\left(-\sigma_m^e(\mathbf{b}) \int_x^L \rho_s(x') dx'\right) dx \quad (3)$$

where  $I^t$  is the measured "transmitted" intensity at the camera [ $\text{W m}^{-2} \text{sr}^{-1}$ ],  $\sigma_m^e(\mathbf{b})$  is the mass-normalized extinction cross-section of the polydisperse soot population [ $\text{m}^2 \text{g}^{-1}$ ] that is a function of eight soot properties represented by the vector  $\mathbf{b}$ ,  $J^s(x, \mathbf{b})$  is a local source radiant intensity per unit mass [ $\text{W sr}^{-1} \text{g}^{-1}$ ] along the measurement path, and the sky-LOSA camera

**Deleted:** as described in Sect. 3.1.3

is located at  $x = L$ . Population-averaged optical properties of soot are computed from the fundamental properties in  $\mathbf{b}$  using Rayleigh–Debye–Gans theory for polydisperse fractal aggregates (RDG–PFA; e.g., Sorensen, 2001). The vector  $\mathbf{b}$  is composed of the absorption function of soot at the measurement wavelength ( $E(m_\lambda)$  [-], where  $m_\lambda$  is the spectral complex refractive index of soot [-]), the scattering-to-absorption function of soot at the measurement wavelength ( $F(m_\lambda)/E(m_\lambda)$  [-]), the monodisperse primary particle diameter of the soot population ( $d_p$  [nm]), the geometric mean soot aggregate size ( $N_g$  [-]), the geometric standard deviation of the lognormal soot aggregate size distribution ( $\sigma_g$  [-]), the diameter-based fractal prefactor ( $k_f$  [-]), the fractal (Hausdorff) dimension ( $D_f$  [-]), and the material density of soot ( $\rho_s$  [ $\text{g cm}^{-3}$ ]). Consistent with laboratory observations of soot structure in the overfire region of flare-like flames (e.g., Köylü and Faeth, 1992), these eight properties are assumed to be spatially and temporally uniform within a single MC draw. However, they are treated as random variables within the sky-LOSA MC method and are in fact the main contributors to overall measurement uncertainties (Johnson et al., 2013). Moreover, it is worth noting that these prior distributions of soot/BC properties inherently link light absorption measurements and computed mass column density/emissions using sky-LOSA. Thus, in keeping with Andreae and Gelencsér (2006) and Petzold et al., (2013), sky-LOSA-inferred soot/BC mass might be called “equivalent BC” as is recommended for all light absorption-based diagnostics.

Deleted: 0

Deleted:  $m$

Deleted:  $m$

Deleted: .

Deleted: While (these eight properties are assumed to be to spatially and temporally uniform within a single MC draw, based on

Deleted: ,

Deleted: t

Deleted: .

Deleted: (

Deleted: ,

Deleted: (

Using mean value theorem, a path-averaged source radiant intensity ( $\bar{J}^s(\mathbf{b})$  [ $\text{W sr}^{-1} \text{g}^{-1}$ ]) can be introduced to simplify the RTE:

$$I^t = I^o \exp\left(-\underbrace{\sigma_m^e(\mathbf{b}) \int_{-\infty}^L \rho_s(x) dx}_{\tau^*}\right) + \frac{\bar{J}^s(\mathbf{b})}{\bar{J}^s} \int_{-\infty}^L \underbrace{\sigma_m^e(\mathbf{b}) \rho_s(x) \exp\left(-\sigma_m^e(\mathbf{b}) \int_x^L \rho_s(x') dx'\right)}_{1-\tau^*} dx \quad (4)$$

where  $\sigma_m^e(\mathbf{b})/\sigma_m^e(\mathbf{b}) = 1$  has also been introduced to the source term. The resulting ratio in front of the second integral represents a path-averaged source intensity ( $\bar{J}^s$  [ $\text{W m}^{-2} \text{sr}^{-1}$ ]) and the exponential in the first term corresponds to the transmittance of the plume in the absence of radiative sources, defined as the idealized transmittance  $\tau^*$  (Johnson et al., 2013).

It can be shown that the integral in the second term is equal to the complement of the idealized transmittance, permitting solution of the latter from the three intensities in Eq. (4):

$$\tau^* = \frac{I^t - \bar{J}^s}{I^o - \bar{J}^s} = \frac{\tau_{obs} - S}{1 - S} \quad (5)$$

where  $\tau_{obs} = I^t/I^o$  is the observed transmittance of the plume [-] and  $S = \bar{J}^s/I^o$  is a term that corrects for brightening of the plume by radiative sources [-]. Noting the definition of the idealized transmittance, the column density of soot is simply:

$$\rho_s'(\tau_{obs}, S, \mathbf{b}) = \frac{-\ln\left(\frac{\tau_{obs} - S}{1 - S}\right)}{\sigma_m^e(\mathbf{b})} \quad (6)$$

In general, the local source radiant intensity ( $J^s(x, \mathbf{b})$ ) is composed of thermal emission and inscattering components. For sky-LOSA however, where measurements are performed in the mid-visible spectrum and plume temperatures are near ambient, thermal emission negligibly contributes to the source term of the RTE (Conrad et al., 2020b). By contrast, diffuse skylight

and direct solar radiation can significantly augment the RTE via inscattering into the optical axis; hence, for sky-LOSA,  $S$  represents an *inscattering correction*. Unfortunately, even if exact knowledge of skylight intensity distribution and solar radiation were available, it is not possible to fully account for the effect of inscattering without prior knowledge of the spatial distribution of soot within the plume. This is because multiple scattering events may occur during light's transmission into the camera. A recent simulation effort, however, has shown that complex multiple scattering effects can be accurately modelled to permit quantification of the inscattering correction ( $S$ ) (Conrad et al., 2020b). This approach requires calculation of the inscattering correction using a *single-scattering assumption* (ISA, subscript "1"):

$$S_1(\alpha_s, \beta, Z_s, a, b) = \underbrace{\int_0^{2\pi} \int_0^{\pi/2} \frac{I(\alpha_s, \beta, Z_s, a) \omega(\mathbf{b})}{I^o(\alpha_s, \beta, Z_s, a)} \frac{1}{4\pi} p(\theta(\alpha_s, \beta, Z), \mathbf{b}) \sin Z dZ da}_{S_{1,sky}(\alpha_s, \beta, Z_s, a, b)} + \underbrace{\frac{E_{sn}(Z_s, a)}{I^o(\alpha_s, \beta, Z_s, a)} \frac{\omega(\mathbf{b})}{4\pi} p(\theta_s(\alpha_s, \beta, Z_s), \mathbf{b})}_{S_{1,sun}(\alpha_s, \beta, Z_s, a, b)} \quad (7)$$

where  $\omega(\mathbf{b})$  is the single-scattering albedo of the polydisperse soot population [-],  $p(\theta; \mathbf{b})$  is the scattering phase function of soot [ $\text{sr}^{-1}$ ], and angles  $\theta$  and  $\theta_s$  represent the angles between the LOS and a region of sky or the sun as shown in Fig. 2. The inscattering correction can be parsed into sky ( $S_{1,sky}$ ) and sun ( $S_{1,sun}$ ) components. Following Conrad et al. (2020b), the ISA-estimated inscattering correction permits calculation of the idealized transmittance – i.e.,  $\tau^* = \tau^*(\tau_{obs}, S_1(\alpha_s, \beta, Z_s, a, \mathbf{b}))$ . Ultimately, this allows for calculation of the soot mass column density by:

$$\rho'_s(\alpha_s, \beta, Z_s, \tau_{obs}, a, \mathbf{b}) = \frac{-\ln \tau^*(\tau_{obs}, S_1(\alpha_s, \beta, Z_s, a, \mathbf{b}))}{\sigma_m^e(\mathbf{b})} \quad (8)$$

According to Eq. (8), sky-LOSA-computation of soot mass column density is a function of the position of the camera and sun, field-observed plume transmittance, skylight intensity distribution and solar irradiance (through  $a$ ), and soot properties. In the sky-LOSA algorithm, uncertainty in soot mass column density is directly calculated by MC analysis over uncertain variables, which include soot properties and other intermediate parameters. This implies that uncertainty in sky-LOSA-computed soot mass column density is sensitive to  $\alpha_s$ ,  $\beta$ ,  $Z_s$ ,  $\tau_{obs}$ , and  $a$ . Of these five variables, only the pointing of the camera may be controlled by the user, through the selection of angles  $\alpha_s$  and  $\beta$ . Critically, these user-selected angles are known to influence sky-LOSA measurement uncertainty and, in extreme cases, can even preclude computation of soot emission rate.

For end-users of sky-LOSA, the sensitivity of measurement uncertainty to camera pointing necessitates a standardized (and ideally simple) data acquisition protocol to optimize camera position and pointing under general conditions. This would allow a priori setup decisions to minimize or constrain uncertainties within reasonable limits. An acquisition protocol must therefore be constructed using quantitative knowledge of measurement uncertainty in sky-LOSA-computed soot mass column density.

Restated in the context of the above theory, the objective of this work is to quantify via a comprehensive general uncertainty

analysis the uncertainty in sky-LOSA-computation of soot mass column density ( $\rho'_s$ ) as a function of user-selectable ( $\alpha_s$  and  $\beta$ ) and uncontrollable parameters ( $Z_s$ ,  $\tau_{obs}$ , and  $a$ ) under generalized conditions. These data permit the development of broad heuristics and, ultimately, an easy-to-use software tool to provide specific case-by-case constraints on camera position and pointing.

### 5 3 General uncertainty analysis methodology

The goal of the present general uncertainty analysis (GUA) is to guide a sky-LOSA user in choosing a sky-LOSA camera position/pointing to minimize measurement uncertainties. The developed software tool can also be used to give an initial estimate of uncertainties in the measured soot emission rate ahead of a more detailed post-processing analysis. To provide generalized recommendations, the GUA quantifies measurement uncertainty in soot mass column density for a selected camera pointing and other independent variables via MC analysis over uncertain variables that include all relevant soot properties.

This section describes the MC method used in the present GUA including novel updates to the MC approach that are necessary to make this present work tractable and significantly accelerate future sky-LOSA analyses.

#### 3.1 Updated Sky-LOSA MC Method

##### 3.1.1 Expansion of the scattering phase function

For a given (modelled) skylight intensity distribution, measured/modelled solar irradiance, camera pointing, and set of soot properties, the ISA-estimated inscattering correction ( $S_1$ ) can be directly calculated via Eq. (7). One significant challenge, and currently the time-limiting computation in sky-LOSA processing, is the calculation of the skylight component ( $S_{1,sky}$ ) via numerical integration over three dimensions:  $\alpha$ ,  $Z$ , and  $N$ , where the latter represents the aggregate size distribution of the soot population. The complexity of this task is exacerbated by the scattering phase function (SPF,  $p(\theta, \mathbf{b})$ ) of soot, which includes a computationally burdensome hypergeometric series in its solution (Sorensen, 2001). For the present GUA, where the inscattering correction must be computed over a five-dimensional domain ( $\alpha_s, \beta, Z_s, a, \mathbf{b}$ ), an alternative, more rapid means of computing the inscattering correction was required to avoid combinatorial explosion.

One such means is through a Fourier-Legendre expansion of the SPF. For an arbitrary set of randomized soot properties  $\mathbf{b}$ , this procedure allows the SPF to be represented as a weighted sum of Legendre polynomials ( $P_l(\cos \theta)$  [-]):

$$p(\theta, \mathbf{b}) = \sum_{l=0}^{\infty} \Phi_l(\mathbf{b}) P_l(\cos \theta) \approx \sum_{l=0}^{L(\mathbf{b})} \Phi_l(\mathbf{b}) P_l(\cos \theta) \quad (9)$$

where  $L(\mathbf{b})$  is the order at which the expansion is truncated [-], and  $\Phi_l(\mathbf{b})$  is the  $l^{\text{th}}$ -order Legendre coefficient [ $\text{sr}^{-1}$ ] (hereinafter termed the  $l^{\text{th}}$ -order soot coefficient) for the set of soot properties ( $\mathbf{b}$ ) computed via:

**Deleted:** the MC method used in the GUA and special considerations ...

**Deleted:**

**Deleted:** s to the

**Deleted:** Special considerations

**Deleted:** for MC analysis

**Deleted:** MC-

**Deleted:** W

**Deleted:**  $P_l(\cos \theta)$  is the  $l^{\text{th}}$ -order Legendre polynomial [-]

$$\Phi_l(\mathbf{b}) = \frac{2l+1}{2} \int_0^\pi p(\theta, \mathbf{b}) P_l(\cos \theta) \sin \theta d\theta \quad (10)$$

which can be accurately and efficiently computed using Gauss-Legendre quadrature (Schuster, 2004). Since the soot coefficient decreases towards zero as the order  $l$  approaches infinity, the infinite series expansion of the SPF can be truncated at a sufficiently large index  $L(\mathbf{b})$  with negligible error (refer to Appendix A section A.1 for further details).

5 Introduction of the Fourier-Legendre-expanded SPF into the sky and sun components of the inscattering correction ( $S_{1,sky}$  and  $S_{1,sun}$ , Eq. (7)) yields:

$$S_{1,sky}(\alpha_s, \beta, Z_s, a, \mathbf{b}) = \frac{\omega(\mathbf{b})}{4\pi} \sum_{l=0}^{L(\mathbf{b})} \Phi_l(\mathbf{b}) \int_0^{2\pi} \int_0^{\frac{\pi}{2}} \underbrace{\frac{I(\alpha, \alpha_s, Z, Z_s, a)}{I^0(\alpha_s, \beta, Z_s, a)} P_l(\cos \theta(\alpha, \beta, Z)) \sin Z dZ da}_{\Psi_{l,sky}(\alpha_s, \beta, Z_s, a)} \quad (11)$$

$$S_{1,sun}(\alpha_s, \beta, Z_s, a, \mathbf{b}) = \frac{\omega(\mathbf{b})}{4\pi} \sum_{l=0}^{L(\mathbf{b})} \Phi_l(\mathbf{b}) \underbrace{\frac{E_{sn}(Z_s, a)}{I^0(\alpha_s, \beta, Z_s, a)} P_l(\cos \theta_s(\alpha_s, \beta, Z_s))}_{\Psi_{l,sun}(\alpha_s, \beta, Z_s, a)} \quad (12)$$

where  $\Psi_{l,sky}(\alpha_s, \beta, Z_s, a)$  and  $\Psi_{l,sun}(\alpha_s, \beta, Z_s, a)$  are denoted as the *sky* and *sun coefficients*, respectively. Importantly, these equations show that use of the expanded SPF removes reference to soot properties from the integral in the computation of  $S_{1,sky}$ , which vastly reduces computational burden. Furthermore, with this formulation, the soot coefficients (functions of  $\mathbf{b}$ ) and sky/sun coefficients (functions of  $\alpha_s, \beta, Z_s,$  and  $a$ ) do not share any independent variables and can therefore be independently pre-computed.

10 While the incident intensity-normalized solar horizontal irradiance ( $E_{sn}(Z_s, a)/I^0(\alpha_s, \beta, Z_s, a)$  [sr]) is typically measured in the field by obtaining neutral density-filtered images of the sun (Johnson et al., 2013), this parameter must be modelled for the GUA. This was accomplished using the CIE sky models and model-dependent typical turbidity factors and diffuse-to-extra-terrestrial solar horizontal irradiance ratios as further detailed in Appendix A section A.2.

### 3.1.2 Sky model categorization

20 The standard CIE sky models have found good utility in a variety of fields, from urban planning (e.g., Acosta et al., 2014) to building design (e.g., Wong, 2017); however, the models naturally suffer from directionally dependent error in skylight intensity. This is particularly true for overcast and partly cloudy skies since the models, which are smooth functions, do not capture steep gradients in skylight intensity due to cloud structures. Thus, there is some additional uncertainty in sky-LOSA-computed soot mass column density through use of a single CIE sky model in the MC method. To permit capture of CIE sky model error in the GUA, like skies were sorted into sky “categories” that have similar properties but differing model coefficients and, hence, directional variability. The derived sky categories ( $a \in \{A \dots D\}$ ) are summarized in Table 1 and can be selected by a sky-LOSA user based on simple observations in the field such as the visibility of the sun (obstructed vs.

Deleted: via

Deleted: <#>Sky and sun inscattering¶

Deleted: <#>Solar irradiance¶

As noted in Sect. 2, ground-level solar normal irradiance –  $E_{sn}(Z_s, a)$ , usually measured via solar images taken in the field – can be modelled using the CIE skylight models. To accomplish this, the incident intensity-normalized solar normal irradiance is expanded:¶

$$\frac{E_{sn}(Z_s, a)}{I^0(\alpha_s, \beta, Z_s, a)} = \frac{E_{sn}(Z_s, a)}{D_h(Z_s, a)} \frac{D_h(Z_s, a)}{I^0(\alpha_s, \beta, Z_s, a)}$$

Deleted: groups

Deleted: selected

Deleted: compiled

Deleted: model

Deleted: groups

Deleted: –

Deleted: t

Deleted: groups



unobstructed) and presence of clouds (overcast, partly cloudy, or clear). By randomly selecting a sky category's component sky models under the MC framework, uncertainty through use of the CIE models is propagated into sky-LOSA-computation of soot mass column density.

Sky category A corresponds to overcast and partly cloudy conditions with an obscured sun. Typical turbidity factors of the component skies ( $T(a)$ ) are high in these conditions, corresponding to low ground-level solar irradiance. Sky category B represents partly cloudy conditions with an unobscured sun where turbidity factors of the component skies are moderate and hemispherical skylight is strong relative to extra-terrestrial solar radiation. Sky categories C and D capture the low-turbidity clear CIE sky models. Sky category C includes all five clear sky models, while sky category D excludes CIE sky type 12, the lowest turbidity (i.e., cleanest atmosphere) model. Sky category D was defined based on the notion that oil and gas activities can be relatively dense geographically. In this case, field experience suggests that local emissions from industrial infrastructure likely precludes CIE sky type 12 as a reasonable model, such that sky category D can be used for the case of clear skies in heavily industrial locales.

### 3.2 MC implementation

Table 2 summarizes the independent, pre-computed, and random variables required to compute soot mass column density under the GUA MC framework. There are five independent variables that define the pointing of the camera relative to the sun ( $\alpha_s, \beta, Z_s$ ), the observed plume transmittance ( $\tau_{obs}$ ), and the skylight intensity distribution (CIE sky type,  $a$ ). Each MC draw randomly chooses soot properties ( $\mathbf{b}$ ) and the scalar multiplier to the sun component of inscattering ( $\xi_{ED}(a)$ , described in Appendix A section A.2). For analyses using the defined sky categories A–D, one CIE sky model is randomly obtained (i.e.,  $a_k$ ) from the selected sky category. The  $k^{\text{th}}$  MC-estimate of the soot mass column density is then calculated via:

$$\rho'_{s,k}(\alpha_s, \beta, Z_s, \tau_{obs}, a_k, \mathbf{b}_k) = \frac{-\ln \tau^* (\tau_{obs}, S_{1,k}(\alpha_s, \beta, Z_s, a_k, \mathbf{b}_k))}{\sigma_m^2(\mathbf{b}_k)} \quad (13)$$

where  $\tau^* (\tau_{obs}, S_{1,k}(\alpha_s, \beta, Z_s, a_k, \mathbf{b}_k))$  is deterministically computed while considering multiple scattering effects, as described by Conrad et al. (2020b), and:

$$S_{1,k}(\alpha_s, \beta, Z_s, a_k, \mathbf{b}_k) = \frac{\omega(\mathbf{b}_k)}{4\pi} \sum_{l=0}^{L(\mathbf{b}_k)} \Phi_l(\mathbf{b}_k) \left( \Psi_{l,sky}(\alpha_s, \beta, Z_s, a_k) + \xi_{ED,k}(a_k) \Psi_{l,sun}(\alpha_s, \beta, Z_s, a_k) \right) \quad (14)$$

In a standard MC analysis, the above procedure would be iterated upon  $K$  times to yield a collection of soot mass column density estimates from which a posterior distribution of soot mass column density could be computed. To accelerate MC procedures in this work, a MC variance reduction technique was employed – specifically, combined multiple Latin hypercube sampling, summarized by Nakayama (2011). This variance reduction technique has been used previously for sky-LOSA (Conrad and Johnson, 2017) and was found to reduce computational burden by a factor of 2–3. For the GUA,  $5 \times 10^5$  (500 sets of 1,000 Latin hypercube-sampled data) MC draws were completed. The GUA MC approach permitted pre-computation

Deleted: the  
Deleted: group's

Deleted: group  
Deleted: where t  
Deleted: ,  
Deleted: group  
Deleted: ET  
Deleted: (high  $D_h(Z_s, a)/E_{sh,o}(Z_s, a)$ )  
Deleted: groups  
Deleted: group  
Deleted: group  
Deleted: group  
Deleted: group

Deleted: ized

Deleted: ,  
Deleted: Moreover, and, f  
Deleted: i  
Deleted: of the  
Deleted: groups  
Deleted: group  
Deleted: obtained  
Deleted: 131317

Deleted: 141418

Deleted: And  $a \equiv a_k$  for analysis of sky groups A–D.

Deleted: (CM-LHS)

Deleted:  
Deleted: CM-LHS

of the soot coefficients, single-scattering albedo, and mass-normalized extinction cross-section for pre-drawn random sets of soot properties (**b**). Parallel pre-computation of the sky and sun coefficients was performed for each of the 15 CIE standard skylight intensity distributions and four sky categories over the angles  $\alpha_s$ ,  $\beta$ , and  $Z_s$  in increments of  $2^\circ$ , and for 18 observed transmittances from 0.25–0.99. This amounted to execution of the MC analysis for almost  $66 \times 10^6$  unique sky-LOSA conditions, permitting derivation of uncertainty statistics over the five independent variables listed in Table 2.

To enable an objective comparison of sky-LOSA uncertainty as a function of the independent variables, a parameter describing the relative uncertainty of MC-computed soot mass column density was required. A natural means of representing relative uncertainty is a coefficient of variation (CV)-like metric that describes a measure of data variance normalized by a measure of central tendency. For consistency with sky-LOSA measurements, a CV-estimator based on the mean and 95% confidence interval was selected for this work. For variability, the width of the 95% CI was scaled by that of the standard normal distribution ( $\approx 3.92$ ) to yield an equivalent standard deviation, while the mean ( $\bar{x}$ ) was employed as the measure of central tendency. The CV-estimator for soot mass column density (or any MC-computed data  $x$ ) was therefore:

$$CV_{95}(x) = \frac{\mathcal{F}_x^{-1}(0.975) - \mathcal{F}_x^{-1}(0.025)}{3.92 \bar{x}} \quad (15)$$

where subscript “95” signifies use of the 95% CI for variability and  $\mathcal{F}_x^{-1}(q)$  is the  $q^{\text{th}}$  quantile of data vector  $x$ .

## 4 Results and discussion

### 4.1 Representative results

Figure 3 shows relative uncertainty results at different camera pointings/positions for an example sky-LOSA measurement scenario of a flare with 90% observed plume transmittance. The selected solar zenith angle ( $Z_s = 32.8^\circ$ ) represents the annual minimum for the Canadian city of Fort St. John, British Columbia, which is located in the Montney oil and gas-producing formation.  $CV_{95}$  data are plotted for sky categories A–D in Figs. 3a–3d, respectively, as a function of relative solar azimuth ( $\alpha_s$  in Fig. 2) and camera inclination ( $\beta$ ); the position of the sun in these coordinates ( $180^\circ, 57.2^\circ$ ) is overlaid in each subfigure. Additionally, contours displaying the solar scattering angle ( $\theta_s$ ) are overlaid in Fig. 3d.

There are two observable trends in the data of Fig. 3 that persist through all measurement conditions. Firstly, the relative uncertainty is a strong function of the solar scattering angle,  $\theta_s$ . This is because of solar radiation’s influence on  $S_{1,sky}$  and  $S_{1,sun}$ . However, the rate at which relative uncertainty changes as a function of  $\theta_s$  is sky model- (as well as solar zenith- and plume transmittance-) dependent. This is partly a consequence of how  $S_{1,sky}$  varies with  $\theta_s$ , but is mostly due to variability in  $S_{1,sun}$  with  $\theta_s$ . For example, the inscattering magnitude for sky category A is effectively due to  $S_{1,sky}$  alone due to high turbidity that strongly attenuates direct solar radiation while, for sky category C, the sun’s inscattering contribution ( $S_{1,sun}$ ) is significant due to the low turbidity of the sky. Thus, the results for sky category A largely represent the effect of  $\theta_s$  on uncertainty through  $S_{1,sky}$  while the results for sky category C include an additional (and the most extreme) effect through

Deleted: CM-LHS MC-r

Deleted: ized

Deleted: groups

Deleted: CM-LHS

Deleted: <#>Relative uncertainty metric¶

Formatted: Indent: First line: 0.2"

Deleted: <#> Since relative uncertainty is a comparison of data variability to central tendency, a natural metric is the coefficient of variation (CV), which is the ratio of the standard deviation to the mean of a distribution or dataset. These moment-based statistics, however, are sensitive to outliers (e.g., Devore and Berk, 2012) or long-tailed/skewed distributions, causing some to suggest order statistics as more-robust metrics for variability and central tendency (e.g., Arachchige et al., 2019). For sky-LOSA

Deleted: <#>, MC- and time-averaged soot mass emission rates (moment-based statistic) have historically been reported alongside MC-computed 95% confidence intervals (CIs, order statistic). Therefore, f

Deleted: <#>past and future

Deleted: <#>se

Deleted: <#>statistics was used in

Deleted: <#>a

Deleted: <#>standard

Formatted: Font: Italic

Deleted: <#>was used as an estimator of the standard deviation

Deleted: <#>i

Deleted: <#> thus

Deleted: 151519

Deleted: groups

Deleted: group

Deleted: group

Deleted: group

Deleted: group

$S_{1,sun}$ . These observations imply that a constraint on  $\theta_s$  is necessary, and that a stricter constraint is required for lower turbidity skies.

The mechanism for the decrease in relative uncertainty with increasing  $\theta_s$  stems from the optical characteristics of soot particulate. Figure 4 shows statistics of the “energy distribution function” ( $EDF = \omega(\mathbf{b})p(\theta, \mathbf{b})/4\pi$ ) discussed by Conrad et al., (2020b), which describes how soot particulate directionally scatters light on an energy-basis. The median and  $CV_{95}$  of the EDF as a function of angle  $\theta$  are shown for the range of the MC-sampled soot properties ( $\mathbf{b}$ ) used in the GUA. This is useful for the present discussion since the EDF contains all soot-dependent variables in the computation of  $S_{1,sun}$  (see Eq. (7)). The figure shows that the EDF, and its influence on  $S_{1,sun}$ , is much larger and much more uncertain as  $\theta_s$  decreases. The influence of these statistics on column density uncertainty depends on the relative intensity of sunlight – specifically  $E_{sn}(Z_s, \alpha)/I^o(\alpha_s, \beta, Z_s, \alpha)$  in Eq. (7). If this value is small (highly turbid skies), then variability in the EDF is less important, but if this value is large (low turbidity skies), then variability in the EDF can dominate relative uncertainty in soot mass column density. Interestingly, relative uncertainty in the EDF approaches a constant value towards  $90^\circ$ . This implies that, regardless of the ground-level intensity of the sun, the uncertainty of  $S_{1,sun}$  becomes minimal at  $\theta_s \gtrsim 90^\circ$  and is within 1% of this minimum for  $\theta_s \gtrsim 60^\circ$  as indicated by the red line in Fig. 4.

The second trend in Fig. 3 that is generally seen across all measurement conditions is the sensitivity of relative uncertainty to the camera inclination angle ( $\beta$ ). Referring to Fig. 3, much of the observed trend in  $\beta$  can likely be attributed to the effect of  $\theta_s$ , since  $\theta_s = \theta_s(\alpha_s, \beta, Z_s)$ . However,  $\beta$  still influences measurement uncertainty as can be observed in the region where the  $\theta_s$  effect is small ( $\theta_s \gtrsim 60^\circ$ ). Figs. 5a through 5e show example trends in soot mass column density uncertainty as a function of  $\beta$  for plume transmittances of 0.25 to 0.95 and a fixed solar azimuth of  $\alpha_s = 60^\circ$ . These figures each plot  $CV_{95}$  as a function of  $\beta$ , averaged over the range of  $Z_s$  that ensures  $\theta_s > 60^\circ$ . The trends are different for each sky model. Uncertainties for sky categories A and B tend to decrease as the camera inclines, while uncertainties for sky categories C and D increase. The severity of these trends increases with plume transmittance (effectively a reduction in the measured signal) and, as plume transmittance increases towards unity, local minima/maxima in uncertainties as a function of camera inclination may appear. The differing influence of  $\beta$  between overcast/partly cloudy and clear sky models is largely due to the specific CIE sky models, which dictate the gradient in skylight intensity near the horizon and the sun. For clear, low-turbidity skies, intensity gradients are large such that small changes in camera pointing can yield significant changes in inscattered light. By contrast, for higher-turbidity skies, gradients are dampened, and the effect of camera pointing is small.

Figure 5 also shows that the  $CV_{95}$  of soot mass column density for sky category C tends to upper bound that of sky category D. This observation holds under most combinations of the MC independent variables and is a result of the somewhat extreme nature of CIE sky model 12 (lowest turbidity / cleanest atmosphere), which is excluded in sky category D. When considered in sky category C however, CIE sky model 12 tends to increase both the variability and central tendency of soot mass column density, but the relative change in the former is larger – hence, inclusion of CIE sky model 12 typically increases relative uncertainty. This implies that sky category C reliably imposes the largest constraints on camera positioning and can therefore

Deleted: (7)(7)

Formatted: English (Canada)

Deleted: (7)(7)

Formatted: English (Canada)

Deleted: groups

Deleted: groups

Deleted: group

Deleted: group

Deleted: group

Deleted: group

Deleted: group

be used to conservatively locate sky-LOSA equipment under clear skies. However, if in a dense industrial area, where the clearest sky model is not relevant, the less-constraining sky [category D](#) can be instead used as noted in Sect. [3.1.2](#).

Deleted: group

Deleted: 3.1.23.1.23.1.5

#### 4.1.1 Camera pointing heuristics

Upon arrival at a measurement facility, the sky-LOSA user's first task is to determine the position of the sky-LOSA camera for data acquisition. This important decision can be made by considering viable camera pointings from GUA MC data through constraints on  $\beta$  and  $\theta_s$ . That is, for a user-identified sky [category](#) and plume transmittance and given the position of the sun, the sky-LOSA camera's pointing can be constrained based on a desired threshold in a relative uncertainty,  $CV_{95}$ . Table 3 provides an example of such constraints. The table lists bounds on the camera inclination angle ( $\beta$ ) and solar scattering angle ( $\theta_s$ ) for each sky [category](#), given the plume transmittance; where bounds were computed by determining where  $CV_{95} \leq 17\%$  for all values of  $Z_s \in [0, 90^\circ]$ , such that the results are independent of solar zenith.

Deleted: group

Deleted: group

One additional consideration in the pointing of the sky-LOSA camera is the direction of plume propagation. Under quiescent conditions, buoyancy-driven flare plumes will propagate vertically away from the flare stack; however, under sufficiently strong crosswinds, the flame and plume can bend over and propagate horizontally, parallel to the wind direction. In this latter case, if the plume propagates towards or away from the sky-LOSA camera, turbulent plume structures of differing vorticity become overlapped from the camera's perspective. Therefore, it is best to position the sky-LOSA camera such that it points orthogonally to the wind direction, which minimizes out-of-image plane motion of the plume and yields the best data for velocimetry calculations. This should be viewed as a weak constraint on sky-LOSA data acquisition however, since the effect of uncertainty in estimated velocity on mass emission rate is generally negligible compared to that of column density uncertainty.

#### 4.1.2 Further camera heuristics

Following selection of a permissible sky-LOSA camera position, the imaging optics must be chosen. Prime (fixed focal length) lenses are employed in the sky-LOSA technique to avoid ambiguity in optical magnification and, hence, spatial scaling of the image. The most appropriate prime lens for the studied flare is one that maintains the entirety of the flare flame well within the image during the data acquisition period. This helps to ensure that a control surface within the image plane that transects the plume and encloses the flame can be derived, as shown in Fig. 1. For a flame that is relatively unsteady – i.e., moving with the wind – it is suggested to keep the flare flame approximately one-quarter of the smallest image dimension. By contrast, if the flame is steady, a flame length of approximately one-third of the smallest image dimension should be targeted. For the sky-LOSA camera used by the authors (minimum sensor dimension of ~14 mm), a good rule-of-thumb is that the appropriate focal length ( $f$ , [mm]) will be on the order of:

$$f[\text{mm}] \approx \frac{4.1}{\cos \beta} \frac{H}{L_f} \quad (16)$$

Deleted: 161620

where  $H$  is the horizontal stand-off distance from the flare stack [m] and  $L_f$  is the length of the flare flame [m]. However, use of a prime lens necessitates a trade-off between lens focal length, horizontal stand-off distance, and size of the flame within the image.

With an appropriate lens selected, the user must then choose imaging parameters that influence the exposure and focus of the image. The objective is to obtain an image that maximizes the digital signal while minimizing exposure time and ensuring the flame is in focus. In the authors' experience, this can be obtained with a lens aperture close to full-open (typically f-number  $\leq 5.6$ ) and an exposure time less than  $\sim 2$  ms. Prior to acquiring the image data, the flame and flare stack should be brought into focus. The user can then obtain sky-LOSA data for the desired duration; it is recommended, however, that a minimum dataset of ten minutes be obtained to permit good convergence of the time-averaged soot emission rate.

#### 10 4.2 Open-source software tool for simpler sky-LOSA setup - *SetupSkyLOSA*

While the camera pointing heuristics presented in Table 3 can be used to ensure that  $CV_{95} \leq 17\%$  for the listed plume transmittances regardless of solar zenith angle, this simplified set of constraints is also necessarily overly conservative and excludes specific combinations of inputs that might produce similar or better uncertainties in different scenarios. An even better approach would be to use the wealth of computed GUA data to provide camera position and pointing constraints on a case-by-case basis. This is made possible using a new open-source software tool, *SetupSkyLOSA* (Conrad, 2020), that was developed as part of this work using the presented GUA MC data. This MATLAB-based application enables a sky-LOSA user to probe statistics of soot mass column density (such as  $CV_{95}$ ) for their specific measurement conditions. The key output of the software tool is an image of the desired soot mass column density statistic plotted as a function of absolute camera pointing. The software tool is briefly described in this section and employed in a case study in Sect. 4.3.

Figure 6 shows a flowchart describing the *SetupSkyLOSA* software's main procedure. For a user-inputted location and time, the software first determines the current position of the sun using an integrated solar position calculator – a MATLAB implementation of the National Renewable Energy Laboratory's (NREL's) Solar Position Algorithm (SPA) (Reda and Andreas, 2008). The SPA returns the solar zenith ( $Z_s$ ) and absolute bearing of the sun ( $\alpha_{sN}$ , where the subscript "N" implies the absolute bearing measured clockwise from *true* North) at the current time and over the measurement date. The user also inputs the index ( $a$ ) of the most appropriate CIE sky model/category, an estimate of the observed plume transmittance at the sky-LOSA measurement wavelength ( $\tau_{obs}$ ), and the desired statistic of soot mass column density ( $\eta$ ). With these inputs, *SetupSkyLOSA* then loads the GUA MC data for the selected sky model/category and interpolates for the desired statistic using the current solar zenith and estimated plume transmittance.

At this point, the software has computed  $\eta(\alpha_s, \beta)$  for the user's current set of independent variables ( $Z_s, \tau_{obs}, a$ ). However, rather than plotting  $\eta(\alpha_s, \beta)$  – i.e., using the relative bearing – the software uses the known absolute bearing of the sun ( $\alpha_{sN}$ , computed by the SPA) to plot  $\eta(\alpha_N, \beta)$ . That is, the requested statistic is plotted as a function of *absolute* camera bearing and inclination, which together define the camera pointing. The user can then easily determine an acceptable camera pointing

Deleted: group

Deleted: group

using a laser rangefinder (for inclination) and a compass (corrected to true North), laser rangefinder, or GPS device (for absolute bearing).

*SetupSkyLOSA* also includes several added utilities to support optimal positioning and pointing of the sky-LOSA camera. Firstly, using the same pinhole camera model that enables spatial scaling of the image, the software tool can optionally overlay the approximate extent of the image sensor in the  $\alpha_N - \beta$  domain, based on sensor dimensions, employed optics, and the pointing of the centre of the image. This helps a user ensure that the entirety of the image frame – including the eventual control surface used for emission rate calculation – has reasonable levels of measurement uncertainty, given a user-selected lens of known focal length. To support ideal velocity calculation, the software can also overlay camera pointings ( $\alpha_N$ ) that are closely orthogonal to the wind. This follows the heuristic discussed in Sect. 4.1.1. The software shows the optimal range of camera pointing as orthogonal to the wind  $\pm 18.2^\circ$ , which corresponds to 5% out-of-image plane motion ( $\cos^{-1}(0.05)$ ). Two additional utilities are not shown in Fig. 6. The “maximizer” utility computes the maximum of a chosen relative uncertainty statistic over a user-defined period. This tool allows a user to seek camera pointings that yield satisfactory uncertainties as the sun moves during the anticipated duration of the sky-LOSA measurement. The “positioner” utility takes the plotted relative uncertainty statistic as a function of camera *pointing* and provides region(s) where the sky-LOSA camera may be *positioned* relative to the flare stack given the flare stack height, maximum horizontal stand-off distance from the flare, and relative uncertainty threshold. The user can optionally print these permissible regions to a *.kml* file for use in mapping software like Google Earth. These latter two utilities are employed in the following case study.

### 4.3 Case study – Atasta facility

The utility of the novel software tool, *SetupSkyLOSA*, is shown in this section via a case study of a sky-LOSA measurement at a real oil and gas facility. The Atasta Gas Processing and Transport Centre (Centro de Proceso y Transporte de Gas Atasta) is a midstream oil and gas facility near Atasta, in the Mexican state of Campeche. The facility is under the jurisdiction of Petróleos Mexicanos and receives sour gas and condensates from the Cantarell offshore oil field for processing and transport to the national market. As shown in Fig. 7a, the Atasta facility is located 35 km West of Ciudad (Cd) del Carmen and approximately 5 km South of the shore of the Bay of Campeche. The facility occupies approximately 1 km<sup>2</sup>, with most infrastructure in the Southeast corner of the site as visible in Fig. 7b. Flaring activities include multiple pit-style and vertical stack flares, which are in the Northwest corner of the site.

For this case study, a sky-LOSA measurement of soot emissions from the central flare stack at the Atasta station was considered as indicated in Fig. 7b, the base of which is located at  $18^\circ 38' 41.46''$  N and  $92^\circ 10' 08.59''$  W. The following example measurement details are assumed:

1. The sky-LOSA measurements occur on May 13, 2021, which is the date of that year that the sun most closely reaches the solar zenith ( $Z_s = 0^\circ$ ).
2. Predicted sky conditions are uncertain and may change between overcast and fully clear conditions throughout the day.

3. Wind speed is predicted to be low and the flare is strongly buoyant.
4. The flare stack is 30 m in height, and the horizontal stand-off distance of the sky-LOSA camera is limited to 250 m or less due to available optics.
5. The flare is lightly sooting, with an observed transmittance of approximately 90% ( $\tau_{obs} \approx 0.90$ ).

5 Assumption #2 implies that sky-LOSA data acquisition may occur under skies represented by any of sky ~~categories A–D~~. Furthermore, assumption #3 suggests that the soot-laden flare plume propagates vertically from the flare stack and, therefore, the constraint on camera position with respect to wind direction is unimportant. The sky-LOSA user wishes to obtain sky-LOSA data with minimal measurement uncertainty, while also avoiding re-location of the sky-LOSA camera throughout the day, if possible.

Deleted: groups

10 Given the known GPS coordinates of the flare stack, measurement date, and the approximate plume transmittance, *SetupSkyLOSA* can be used to constrain sky-LOSA camera pointing for any sky condition and time of the day based on the  $CV_{95}$  of soot mass column density. Since the user wishes to avoid re-location of the sky-LOSA camera, camera position and pointing should be constrained using the relative uncertainty maximized over the day. The “maximizer” utility of *SetupSkyLOSA* permits this calculation for each of the sky ~~categories~~; results are shown in Fig. 8a–8d for sky ~~categories A–D~~.  
15 Noting the differing colour scales in the four figures, there is significant variability in sky-LOSA uncertainties for each of the sky ~~categories~~, as in Fig. 3. For further context, the path of the sun over the measurement date is overlaid in Fig. 8a–8d in addition to a contour of  $CV_{95} = 16.5\%$ , which is within 1% of the best attainable uncertainty for these conditions.

Deleted: groups

Deleted: groups

Deleted: groups

Using the uncertainty data in Fig. 8a–8d, the “positioner” utility of *SetupSkyLOSA* can be employed to highlight where the sky-LOSA camera may be positioned relative to the flare stack. This was performed for each of the sky ~~categories~~ using the uncertainty threshold of 16.5%. Permissible camera positions were output in *.kml* format by the “positioner” utility and are overlaid on a map of the Atasta facility in Fig. 8e and are quite different for each of the sky ~~categories~~. Permissible camera positions for sky ~~category B~~ exist beyond a small region near the stack tip, while those for sky ~~category A~~ are within an annular region surrounding the flare stack – since the lower limit on the camera inclination angle in Fig. 8a imposes a maximum permissible stand-off distance. Sky ~~category D~~ contains two permissible regions – one to the South and one to the North of the flare stack – while the most-constrained sky ~~category C~~ has one relatively small region to the North of the flare stack.

Deleted: groups

Deleted: groups

Deleted: group

Deleted: group

Deleted: group

Deleted: group

25 Recalling assumption #2, that predicted sky conditions were uncertain, the sky-LOSA user should ideally position the camera at the intersection of the sky ~~category~~-dependent permissible regions. This small area is outlined in black in the figure, is ~136 m due North of the flare stack and is just 604 m<sup>2</sup> in size (~0.31% of the 250 m radius region). It is apparent in Fig. 8e that this ideal position intersects a clearing in the treed area where the sky-LOSA camera should be positioned for the specific conditions of this case study.

Deleted: group

30 This case study shows the remarkable utility of the *SetupSkyLOSA* software tool. The tool quickly provides resolved measurement uncertainty data from the GUA that would otherwise require millions of MC analyses to compute. These uncertainty data enable optimal sky-LOSA camera positioning and pointing and also represent a first-order estimate of soot emission rate uncertainties that are computed in post-processing. Together with the additional utilities and general camera

heuristics, this software tool permits a sky-LOSA user to obtain optimal sky-LOSA data that minimizes measurement uncertainties under generalized conditions.

## 5 Conclusions

A comprehensive Monte Carlo-based general uncertainty analysis (GUA) has been used to develop heuristics constraining the pointing/positioning of sky-LOSA equipment for measurement of soot/black carbon emissions from gas flares. The GUA identifies generalized constraints based on predicted measurement uncertainties in soot mass column density, computed using sky-LOSA. The results show that equipment setup constraints can be classified based on the conditions of the sky, relative positioning of the sun, and inclination angle of the camera. With additional heuristics on camera optics and imaging parameters, the presented results provide generalized guidance to greatly simplify acquisition of optimal sky-LOSA data in the context of complex, non-linear measurement uncertainties. These are further extended in the open-source software utility, *SetupSkyLOSA*, which interprets the GUA results to provide detailed guidance for any specific combination of location, date/time, and flare, plume, and ambient conditions. Furthermore, software-displayed soot mass column density statistics provide the user with a first-order estimate of measurement uncertainty in soot/black carbon emission rate that otherwise is only computable during post-processing. The case study using *SetupSkyLOSA* to identify optimal equipment setup at a real oil and gas facility in Mexico demonstrates the utility of this new software tool, which as an open-source application can hopefully facilitate broader use of the sky-LOSA technique and ultimately help increase the knowledge base of soot/black carbon emissions from gas flares.

### Data availability

The developed software tool and associated data are available online as open-source and build distributions ([doi: 10.5281/zenodo.3908540](https://doi.org/10.5281/zenodo.3908540); Conrad, 2020).

### Author contribution

Both authors conceptualized the research and developed the methodology. MJ was responsible for funding acquisition, project administration, provision of resources, and supervision. BC curated the data, performed the formal analysis and investigation, developed the software, and produced the original manuscript including visualizations. Both authors reviewed and edited the manuscript throughout the publication process.

### Competing interests

The authors declare that they have no conflict of interest.



## Acknowledgements

This work was supported by the Natural Sciences and Engineering Research Council of Canada (NSERC) FlareNet Strategic Network (Grant #479641), NSERC Discovery Research Grants (Grant #06632 and 522658), and Natural Resources Canada (Project Manager, Michael Layer). We are grateful to Dr. Brian Crosland (Natural Resources Canada) for supplying computational resources.

## Appendix A Implementation details of the updated MC method

### A.1 Truncation of the expanded SPF

For the prior probability distributions of soot properties derived by Johnson et al. (2013), the total order of soot coefficients required to represent the soot SPF according to the procedure of Schuster (2004) was typically  $L(\mathbf{b}) = 76$  (median). In the most extreme case however, representing a strongly forward scattering soot population (corresponding to large soot aggregate size),  $L(\mathbf{b})$  reached 698, suggesting that pre-computation of the sky and sun coefficients up to  $\Psi_{698}$  would be necessary to compute the inscattering correction in the worst case. While calculation of the sun coefficients to this large order is generally trivial, calculation of the sky coefficients becomes overwhelmingly cumbersome as the order increases. Importantly though, like the soot coefficients, the magnitude of the sky coefficients approaches zero as the order approaches infinity; therefore, the product of  $\Phi_l(\mathbf{b})$  and  $\Psi_{l,sky}(\alpha_s, \beta, Z_s, \mathbf{a})$  more-rapidly decreases in magnitude as  $l$  increases than either component alone. This permits further truncation of the series for the calculation of  $S_{1,sky}$ . Specifically, calculation of  $S_{1,sky}$  via Eq. (11) using  $L(\mathbf{b}) = 200$  was consistently in close agreement with direct numerical integration via Eq. (7) – where, over  $10^6$  randomized sets of  $(\alpha_s, \beta, Z_s, \mathbf{a}, \mathbf{b})$ , the median relative difference was just  $2.3 \times 10^{-7}$ . This implies that it is acceptable to impose that  $\Psi_{l,sky}(\alpha_s, \beta, Z_s, \mathbf{a}) = 0, \forall l > 200$ .

### A.2 Incident intensity-normalized solar normal irradiance

As noted in Sect. 2, ground-level solar normal irradiance –  $E_{sn}(Z_s, \mathbf{a})$ , usually measured via solar images taken in the field – can be modelled using the CIE skylight models. To accomplish this, the incident intensity-normalized solar normal irradiance is expanded:

$$\frac{E_{sn}(Z_s, \mathbf{a})}{I^o(\alpha_s, \beta, Z_s, \mathbf{a})} = \frac{E_{sn}(Z_s, \mathbf{a})}{D_h(Z_s, \mathbf{a})} \frac{D_h(Z_s, \mathbf{a})}{I^o(\alpha_s, \beta, Z_s, \mathbf{a})} \quad (\text{A.1})$$

where  $D_h(Z_s, \mathbf{a})$  is the diffuse horizontal irradiance, calculable for the CIE models via numerical integration of:

$$D_h(Z_s, \mathbf{a}) = \int_0^{2\pi} \int_0^{\frac{\pi}{2}} I(\alpha, \alpha_s, Z, Z_s, \mathbf{a}) \cos Z \sin Z \, dZ \, d\alpha \quad (\text{A.2})$$

which is independent of the value of  $\alpha_s$ .

The ratio of solar normal to diffuse horizontal irradiance is complex to quantify in a general sense as it is a function of atmospheric composition. However, for the purposes of the present GUA it is modelled as follows:

$$\frac{E_{sn}(Z_s, a)}{D_h(Z_s, a)} = \frac{E_{sh,o}(Z_s, a) \exp(-m(Z_s)\sigma^{e^*}(m)T(a))}{D_h(Z_s, a) \cos Z_s} \quad (A.3)$$

The numerator of the righthand side is the ground-level solar horizontal irradiance, calculated as the product of the extra-terrestrial (subscript “o”) solar horizontal irradiance ( $E_{sh,o}(Z_s, a)$ ) with an exponential representing attenuation through the atmosphere. In computation of the latter,  $m(Z_s)$  is the relative air mass quantifying the amount of air in the atmosphere at the solar zenith angle relative to the vertical direction,  $\sigma^{e^*}(m)$  is the ideal extinction for a clean atmosphere at a given relative air mass, and  $T(a)$  is the model-dependent turbidity factor that is used to consider realistic atmospheres and describes the number of clean atmospheres required to represent attenuation through the non-ideal, polluted atmosphere. In the denominator, the cosine is included to transform the numerator into the required ground-level solar *normal* irradiance. In the present work, typical values of the turbidity factor ( $T(a)$ ) and irradiance ratio  $D_h(Z_s, a)/E_{sh,o}(Z_s, a)$  are taken from Darula and Kittler (2002) and Kittler et al. (2012), while their recommended formulations for  $m(Z_s)$  (Kasten and Young, 1989) and  $\sigma^{e^*}(m)$  (Navvab et al., 1984) are employed:

$$\begin{aligned} m(Z_s) &= (\cos Z_s + 0.50572(96.07995^\circ - Z_s)^{-1.6364})^{-1} \\ \sigma^{e^*}(m) &= (9.9 + 0.043m)^{-1} \end{aligned} \quad (A.4)$$

To model some amount of unknown uncertainty due to the use of “typical” metrics listed in the literature, an additional randomized variable ( $\xi_{ED}(a)$ ) was introduced as a scalar multiplier to the sun component of the inscattering correction. For CIE sky models with an unobstructed sun (types 7–15),  $\xi_{ED}(a) \sim \mathcal{U}(0.75, 1.25)$  and for models with an obstructed sun (types 1–6),  $\xi_{ED}(a) \sim \mathcal{U}(0, 1.25)$ . These prior distributions of  $\xi_{ED}(a)$  were based on observations by Watanabe et al. (2016), who studied the “clearness index” (ground-level horizontal normalized by extra-terrestrial horizontal irradiance) over five years at 47 observation stations across Japan. They found that the relative variation in the clearness index was approximately 4.3% for skies with unobscured suns and 35% for skies with obscured suns; corresponding variance-equivalent uniform distributions would have a range of 15% and 121%, respectively. For skies with an unobscured sun, this range was expanded to 50% (0.75–1.25) to give a conservatively broad prior since measurement uncertainty can be quite sensitive to solar irradiance. By contrast, for skies with an obscured sun, where the solar irradiance has a small contribution to measurement uncertainty, the uniform distribution was only slightly widened to 125% (0–1.25).

## References

- Acosta, I., Navarro, J. and Sendra, J. J.: Lighting design in courtyards: Predictive method of daylight factors under overcast sky conditions, *Renew. Energy*, 71, 243–254, doi:10.1016/j.renene.2014.05.020, 2014.
- Allen, D. T. and Torres, V. M.: TCEQ 2010 Flare study final report, Texas Commission on Environmental Quality (TCEQ),

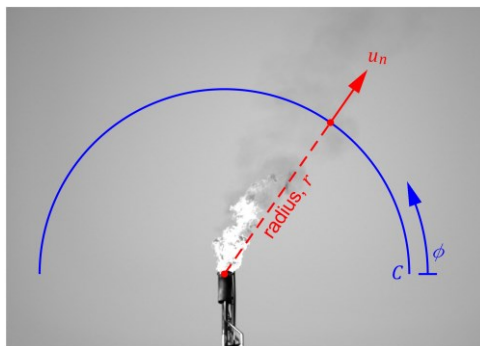
- Austin, TX. [online] Available from: <http://www.tceq.texas.gov/assets/public/implementation/air/rules/Flare/2010flarestudy/2010-flare-study-final-report.pdf>, 2011.
- Andreae, M. O. and Gelencsér, A.: Black carbon or brown carbon? The nature of light-absorbing carbonaceous aerosols, *Atmos. Chem. Phys.*, 6(10), 3131–3148, doi:10.5194/acp-6-3131-2006, 2006.
- 5 Anenberg, S. C., Schwartz, J., Shindell, D., Amann, M., Faluvegi, G., Klimont, Z., Janssens-Maenhout, G., Pozzoli, L., Van Dingenen, R., Vignati, E., Emberson, L., Müller, N. Z., West, J. J., Williams, M., Demkine, V., Hicks, W. K., Kuylenstierna, J., Raes, F. and Ramanathan, V.: Global Air Quality and Health Co-benefits of Mitigating Near-Term Climate Change through Methane and Black Carbon Emission Controls, *Environ. Health Perspect.*, 120(6), 831–839, doi:10.1289/ehp.1104301, 2012.
- 10 Becker, H. A. and Liang, D.: Total emission of soot and thermal radiation by free turbulent diffusion flames, *Combust. Flame*, 44(1–3), 305–318, doi:10.1016/0010-2180(82)90080-3, 1982.
- Bond, T. C., Doherty, S. J., Fahey, D. W., Forster, P. M., Bernsten, T. K., DeAngelo, B. J., Flanner, M. G., Ghan, S., Kärcher, B., Koch, D., Kinne, S., Kondo, Y., Quinn, P. K., Sarofim, M. C., Schultz, M. G., Schulz, M., Venkataraman, C., Zhang, H., Zhang, S., Bellouin, N., Guttikunda, S. K., Hopke, P. K., Jacobson, M. Z., Kaiser, J. W., Klimont, Z., Lohmann, U.,
- 15 Schwarz, J. P., Shindell, D. T., Storelvmo, T., Warren, S. G. and Zender, C. S.: Bounding the role of black carbon in the climate system: A scientific assessment, *J. Geophys. Res. Atmos.*, 118(11), 5380–5552, doi:10.1002/jgrd.50171, 2013.
- CIE: Spatial Distribution of Daylight - CIE Standard General Sky, Commission Internationale de l'Éclairage, Vienna, Austria., 2003.
- Conrad, B. M.: SetupSkyLOSA: A MATLAB Tool to support Acquisition of Sky-LOSA Data, , doi:10.5281/zenodo.3908540,
- 20 2020.
- Conrad, B. M. and Johnson, M. R.: Field measurements of black carbon yields from gas flaring, *Environ. Sci. Technol.*, 51(3), 1893–1900, doi:10.1021/acs.est.6b03690, 2017.
- Conrad, B. M. and Johnson, M. R.: Mass absorption cross-section of flare-generated black carbon: Variability, predictive model, and implications, *Carbon N. Y.*, 149, 760–771, doi:10.1016/j.carbon.2019.04.086, 2019.
- 25 Conrad, B. M., Thornock, J. N. and Johnson, M. R.: Beam steering effects on remote optical measurements of pollutant emissions in heated plumes and flares, *J. Quant. Spectrosc. Radiat. Transf.*, 254, doi:10.1016/j.jqsrt.2020.107191, 2020a.
- Conrad, B. M., Thornock, J. N. and Johnson, M. R.: The effect of multiple scattering on optical measurement of soot emissions in atmospheric plumes, *J. Quant. Spectrosc. Radiat. Transf.*, 254, 107220, doi:10.1016/j.jqsrt.2020.107220, 2020b.
- Darula, S. and Kittler, R.: Cie general sky standard defining luminance distributions, Bratislava, Slovakia., 2002.
- 30 Elvidge, C. D., Baugh, K. E., Tuttle, B. T., Howard, A. T., Pack, D. W., Milesi, C. and Erwin, E. H.: A Twelve Year Record of National and Global Gas Flaring Volumes Estimated Using Satellite Data: Final Report to the World Bank., 2007.
- Elvidge, C. D., Ziskin, D., Baugh, K. E., Tuttle, B. T., Ghosh, T., Pack, D. W., Erwin, E. H. and Zhizhin, M.: A Fifteen Year

- Record of Global Natural Gas Flaring Derived from Satellite Data, *Energies*, 2(3), 595–622, doi:10.3390/en20300595, 2009.
- Elvidge, C. D., Zhizhin, M., Baugh, K., Hsu, F. and Ghosh, T.: Methods for global survey of natural gas flaring from visible infrared imaging radiometer suite data, *Energies*, 9(1), 14, doi:10.3390/en9010014, 2016.
- 5 Gvakharia, A., Kort, E. A., Brandt, A. R., Peischl, J., Ryerson, T. B., Schwarz, J. P., Smith, M. L. and Sweeney, C.: Methane, black carbon, and ethane emissions from natural gas flares in the Bakken Shale, North Dakota, *Environ. Sci. Technol.*, 51(9), 5317–5325, doi:10.1021/acs.est.6b05183, 2017.
- Jacobson, M. Z.: Strong radiative heating due to the mixing state of black carbon in atmospheric aerosols, *Nature*, 409(6821), 695–697, doi:10.1038/35055518, 2001.
- 10 Johnson, M. R., Wilson, D. J. and Kostiuik, L. W.: A fuel stripping mechanism for wake-stabilized jet diffusion flames in crossflow, *Combust. Sci. Technol.*, 169(1), 155–174, doi:10.1080/00102200108907844, 2001.
- Johnson, M. R., Devillers, R. W., Yang, C. and Thomson, K. A.: Sky-Scattered solar radiation based plume transmissivity measurement to quantify soot emissions from flares, *Environ. Sci. Technol.*, 44(21), 8196–8202, doi:10.1021/es1024838, 2010.
- 15 Johnson, M. R., Devillers, R. W. and Thomson, K. A.: Quantitative field measurement of soot emission from a large gas flare using sky-LOSA, *Environ. Sci. Technol.*, 45(1), 345–350, doi:10.1021/es102230y, 2011.
- Johnson, M. R., Devillers, R. W. and Thomson, K. A.: A generalized sky-LOSA method to quantify soot/black carbon emission rates in atmospheric plumes of gas flares, *Aerosol Sci. Technol.*, 47(9), 1017–1029, doi:10.1080/02786826.2013.809401, 2013.
- 20 Kasten, F. and Young, A. T.: Revised optical air mass tables and approximation formula., *Appl. Opt.*, 28(22), 4735–4738 [online] Available from: <http://linkinghub.elsevier.com/retrieve/pii/0378778884900616>, 1989.
- Kittler, R., Kocifaj, M. and Darula, S.: *Daylight Science and Daylighting Technology*, Springer New York, New York, NY., 2012.
- Köylü, Ü. Ö. and Faeth, G. M.: Structure of overfire soot in buoyant turbulent diffusion flames at long residence times, 25 *Combust. Flame*, 89(2), 140–156, doi:10.1016/0010-2180(92)90024-J, 1992.
- McDaniel, M.: Flare efficiency study, United States Environmental Protection Agency, Research Triangle Park, NC. [online] Available from: <http://nepis.epa.gov/Exe/ZyPURL.cgi?Dockey=P1003QGZ.txt>, 1983.
- McEwen, J. D. N. and Johnson, M. R.: Black carbon particulate matter emission factors for buoyancy-driven associated gas flares, *J. Air Waste Manage. Assoc.*, 62(3), 307–321, doi:10.1080/10473289.2011.650040, 2012.
- 30 Nakayama, M. K.: Asymptotically Valid Confidence Intervals for Quantiles and Values-at-Risk When Applying Latin Hypercube Sampling, *Int. J. Adv. Syst. Meas.*, 4(1), 86–94, 2011.

- Navvab, M., Karayel, M., Ne'eman, E. and Selkowitz, S.: Analysis of atmospheric turbidity for daylight calculations, *Energy Build.*, 6(3), 293–303, doi:10.1016/0378-7788(84)90061-6, 1984.
- Petzold, A., Ogren, J. A., Fiebig, M., Laj, P., Li, S.-M., Baltensperger, U., Holzer-Popp, T., Kinne, S., Pappalardo, G., Sugimoto, N., Wehrli, C., Wiedensohler, A. and Zhang, X.-Y.: Recommendations for reporting “black carbon” measurements, *Atmos. Chem. Phys.*, 13(16), 8365–8379, doi:10.5194/acp-13-8365-2013, 2013.
- Pohl, J. H., Tichenor, B. A., Lee, J. and Payne, R.: Combustion Efficiency of Flares, *Combust. Sci. Technol.*, 50(4–6), 217–231, doi:10.1080/00102208608923934, 1986.
- Popovicheva, O. B., Evangelidou, N., Eleftheriadis, K., Kalogridis, A. C., Sitnikov, N., Eckhardt, S. and Stohl, A.: Black Carbon Sources Constrained by Observations in the Russian High Arctic, *Environ. Sci. Technol.*, 51(7), 3871–3879, doi:10.1021/acs.est.6b05832, 2017.
- Ramanathan, V. and Carmichael, G.: Global and regional climate changes due to black carbon, *Nat. Geosci.*, 1(4), 221–227, doi:10.1038/ngeo156, 2008.
- Reda, I. and Andreas, A.: *Solar Position Algorithm for Solar Radiation Applications (Revised)*, Golden, CO (United States), 2008.
- Sato, M., Hansen, J., Koch, D., Lacis, A., Ruedy, R., Dubovik, O., Holben, B., Chin, M. and Novakov, T.: Global atmospheric black carbon inferred from AERONET, *Proc. Natl. Acad. Sci.*, 100(11), 6319–6324, doi:10.1073/pnas.0731897100, 2003.
- Schuster, G. L.: *Inferring the Specific Absorption and Concentration of Black Carbon From Aeronet Aerosol Retrievals*, Pennsylvania State University., 2004.
- Sorensen, C. M.: Light Scattering by Fractal Aggregates: A Review, *Aerosol Sci. Technol.*, 35(2), 648–687, doi:10.1080/02786820117868, 2001.
- Stohl, A., Berg, T., Burkhart, J. F., Fjærraa, A. M., Forster, C., Herber, A., Hov, Ø., Lunder, C., McMillan, W. W., Oltmans, S., Shiobara, M., Simpson, D., Solberg, S., Stebel, K., Ström, J., Tørseth, K., Treffeisen, R., Virkkunen, K. and Yttri, K. E.: Arctic smoke – record high air pollution levels in the European Arctic due to agricultural fires in Eastern Europe, *Atmos. Chem. Phys. Discuss.*, 6(5), 9655–9722, doi:10.5194/acpd-6-9655-2006, 2006.
- Trivanovic, U., Sipkens, T. A., Kazemimanesh, M., Baldelli, A., Jefferson, A. M., Conrad, B. M., Johnson, M. R., Corbin, J. C., Olfert, J. S. and Rogak, S. N.: Morphology and size of soot from gas flares as a function of fuel and water addition, *Fuel*, 279, 1–10, doi:10.1016/j.fuel.2020.118478, 2020.
- U.S. EPA: AP 42 - Compilation of Air Pollutant Emission Factors, Volume I, Section 13.5 Industrial Flares, Research Triangle Park, NC. [online] Available from: <https://www3.epa.gov/ttn/chief/ap42/ch13/index.html>, 2018.
- United Nations Economic Commission for Europe: 1999 Protocol to Abate Acidification, Eutrophication and Ground-level ozone to the Convention on Long-range Transboundary Air Pollution., 2012.
- Watanabe, T., Takamatsu, T. and Nakajima, T. Y.: Evaluation of Variation in Surface Solar Irradiance and Clustering of

- Observation Stations in Japan, *J. Appl. Meteorol. Climatol.*, 55(10), 2165–2180, doi:10.1175/JAMC-D-15-0227.1, 2016.
- Weyant, C. L., Shepson, P. B., Subramanian, R., Cambaliza, M. O. L. L., Heimburger, A., McCabe, D., Baum, E., Stirr, B. H. and Bond, T. C.: Black carbon emissions from associated natural gas flaring, *Environ. Sci. Technol.*, 50(4), 2075–2081, doi:10.1021/acs.est.5b04712, 2016.
- 5 Wieneke, B.: PIV uncertainty quantification from correlation statistics, *Meas. Sci. Technol.*, 26(7), 074002, doi:10.1088/0957-0233/26/7/074002, 2015.
- Wong, I. L.: A review of daylighting design and implementation in buildings, *Renew. Sustain. Energy Rev.*, 74, 959–968, doi:10.1016/j.rser.2017.03.061, 2017.

## 10 Figures and Tables



- Figure 1: Sample sky-LOS image of the flare and atmospheric plume, which is under slight crosswind in this example. A control surface ( $C$ ) is shown in blue, which is defined by its constant radius ( $r$ ) and the angle  $\phi$ . At each point on the control surface, the mass column density ( $\rho'_s(r, \phi)$ , not shown) is computed via careful consideration of radiative effects along the lines-of-sight (perpendicular to the image plane) that compose the control surface. Additionally, the path-averaged normal plume velocity ( $u_n(r, \phi)$ ) is computed via image correlation velocimetry. The instantaneous mass emission rate is computed by integrating the product of these over the control surface defined by  $rd\phi$ .
- 15

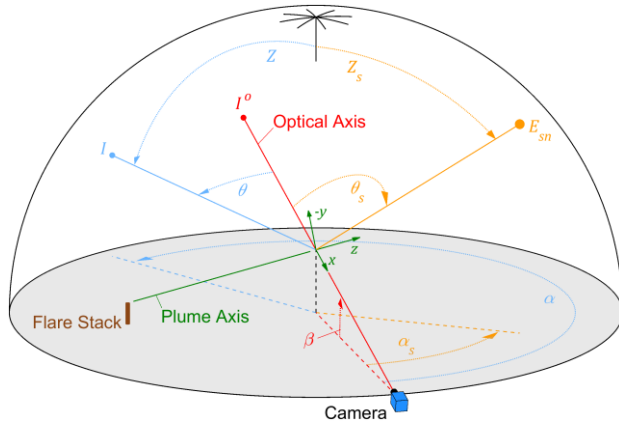


Figure 2: Schematic of a sky-LOSA measurement under the hemispherical sky dome showing the camera's optical axis relative to the horizon ( $\beta$ ), sun ( $\alpha_s$ ,  $\theta_s$ , and  $Z_s$ ), and example sky element ( $\alpha$ ,  $\theta$ ,  $Z$ ) (adapted from Conrad et al., 2020).

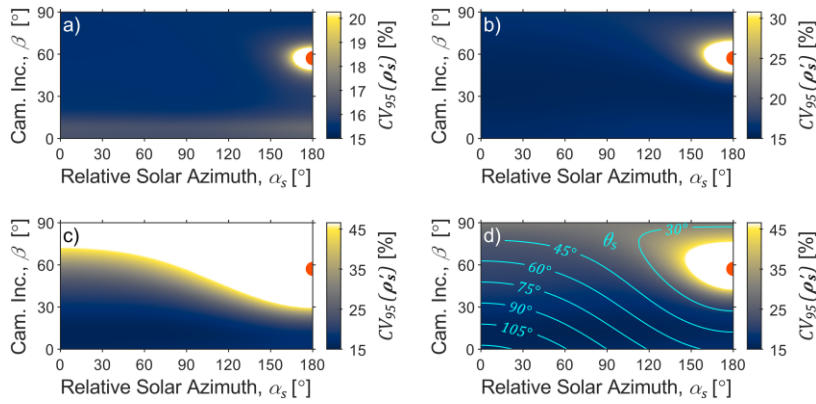


Figure 3: Example MC results at solar noon on the summer solstice in Fort St. John, British Columbia – solar zenith ( $Z_s$ ) of  $32.8^\circ$  – for a plume of 90% observed plume transmittance ( $\tau_{obs}$ ). Subplots (a)–(d) show the relative uncertainty ( $CV_{95}$ ) of soot mass column density as a function of relative solar azimuth ( $\alpha_s$ ) and camera inclination ( $\beta$ ) for sky categories A–D, respectively. Contour lines in subplot (d) show the scattering angle of sunlight into the sky-LOSA camera ( $\theta_s$ ).

Deleted: groups

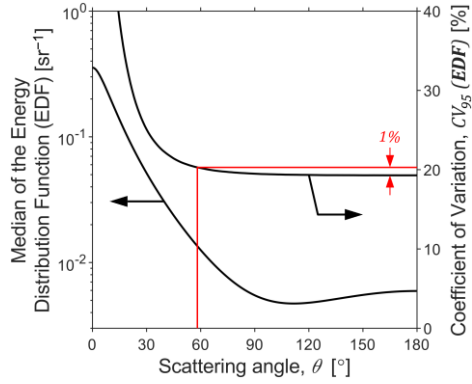


Figure 4: Central tendency (median; left logarithmic axis) and relative uncertainty ( $CV_{95}$ ; right linear axis) of the “energy distribution function” ( $EDF = \omega(b)p(\theta, b)/4\pi$ ) that dictates the fraction of incident light energy scattered through angle  $\theta$  by soot. The magnitude and uncertainty in the EDF are much larger in the forward scattering direction (small  $\theta$ ). As the scattering direction exceeds  $\sim 90^\circ$  however, the relative uncertainty in the EDF approaches a constant minimum, implying that the relative uncertainty in  $S_{1, sun}$  is minimized for  $\theta_s \gtrsim 90^\circ$ . The red line shows that relative uncertainty is within 1% of the minimum if  $\theta_s \gtrsim 60^\circ$ .



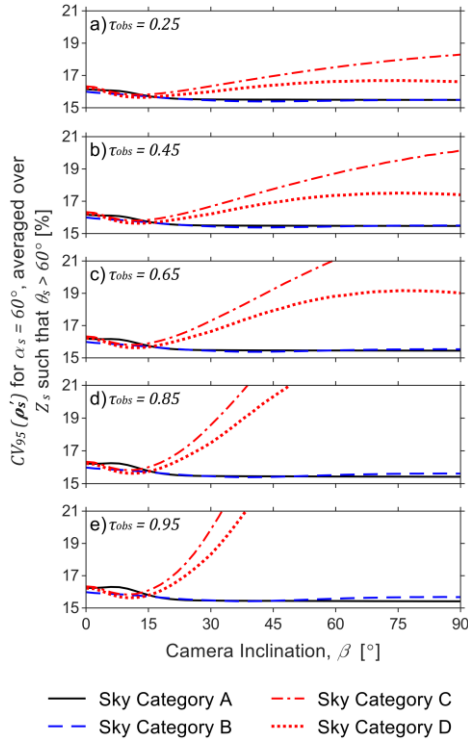


Figure 5: Percentage relative uncertainty in soot mass column density for a relative solar azimuth ( $\alpha_s$ ) of  $60^\circ$  averaged over all solar zenith angles ( $Z_s$ ) as a function of camera inclination angle ( $\beta$ ). Data are plotted for each sky category for observed transmittances ( $\tau_{obs}$ ) of 0.25 to 0.95 in subplots (a)–(e). For sky categories A and B (representing overcast and partly cloudy skies), uncertainty can be slightly reduced by ensuring the camera inclination angle exceeds approximately  $15^\circ$ . For sky categories C and D (representing clear skies), minimal uncertainty is achieved at camera inclination of  $9.75$ – $12.50^\circ$ , and uncertainty can drastically increase for camera inclination increase beyond  $20^\circ$  – however, the effect becomes muted for more optically thick plumes (lower  $\tau_{obs}$ ). These observations support the general heuristic for clear skies that the camera inclination angle should be kept below  $\sim 20^\circ$ , especially for lightly and moderately sooting flares.

Deleted: group

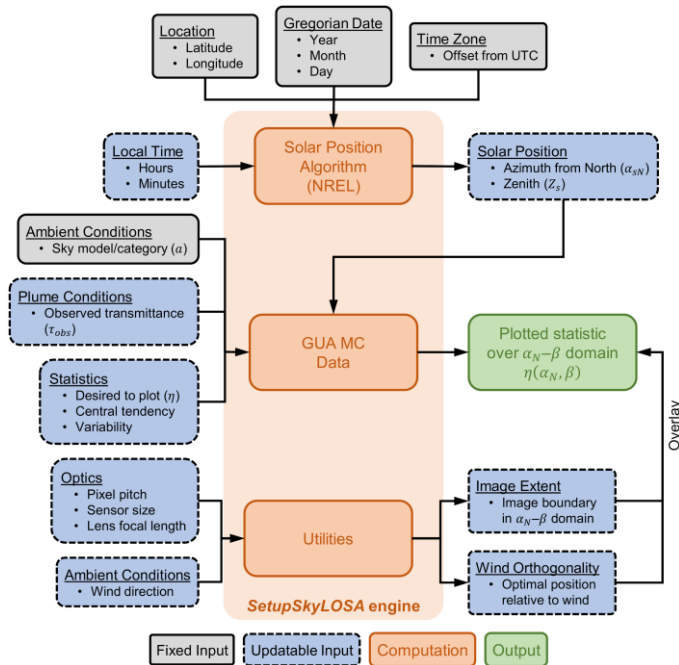


Figure 6: Flowchart of the main procedure of the *SetupSkyLOSA* software tool. The user provides the location, Gregorian date, time zone, and local time, which are used to compute the corresponding solar position using the Solar Position Algorithm of the National Renewable Energy Laboratory (NREL, Reda and Andreas, 2008). Then, with data on ambient conditions and observed plume transmittance, the software tool plots the desired statistic of soot mass column density over the  $\alpha_N - \beta$  domain. Additional utilities include the overlay of the image sensor and optimal positioning relative to the wind on the plotted statistic, in addition to the “maximizer” and “positioner” utilities, which are not shown in the figure. The latter two utilities permit a user to identify acceptable camera positions/pointings over a measurement period and output this data in .kml format for use with mapping software such as Google Earth.



Figure 7: (a) Location of the Atasta Gas Processing and Transport Centre in the Mexican state of Campeche, 35 km West of Ciudad (Cd) del Carmen and approximately 5 km South of the Bay of Campeche. (b) Location of the flare that is the focus of the case study located in the Northwest corner of the site amongst other flaring infrastructure.

5

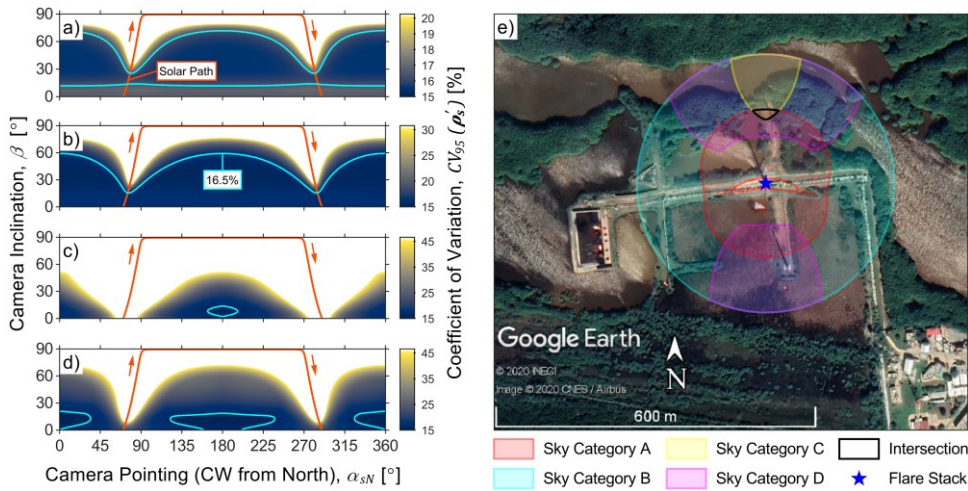


Figure 8: (a–d) Relative uncertainty ( $CV_{95}$ ) in soot mass column density as a function of camera inclination ( $\beta$ ) and pointing ( $\alpha_{SN}$ ), maximized over the measurement day for sky categories A–D, respectively, given an observed plume transmittance ( $\tau_{obs}$ ) of 0.90. Overlaid in the figures is the path of the sun over the day (which approximately reaches  $Z_s = 0^\circ$  at 13:05 Central Daylight Time) in addition to a contour of  $CV_{95} = 16.5\%$ . (e) Permissible regions for sky-LOSA camera positioning relative to the studied flare stack for sky categories A–D. The black line shows the intersection of these regions which is a  $\sim 600 \text{ m}^2$  that the sky-LOSA camera can be positioned to minimize measurement uncertainty, regardless of sky conditions.

10

Deleted: groups

Deleted: groups

Table 1: Sky categories, derived to propagate error in the CIE sky models through the sky-LOSA algorithm computing soot mass column density.

Sky Category	CIE Sky Types ( $\alpha$ )	Description
A	1–6	Overcast and partly cloudy skies, obscured sun
B	7–10	Partly cloudy skies, unobscured sun
C	11–15	Clear skies, all
D	11, 13–15	Clear skies, polluted

Deleted: model

Deleted: "groups"

Deleted: Group

Table 2: Summary of independent, random, and pre-computed variables in the GUA.

Variable Group	Variable Name	Symbol	Unit	Source <sup>a</sup>	GUA MC Implementation <sup>b</sup>
Ambient lighting	Sky model coefficients	$a_k$	[-]	CIE models	Independent/ random
	Skylight intensity	$I(\alpha_s, \beta, Z_s, a)$	[W m <sup>-2</sup> sr <sup>-1</sup> ]		
	Incident skylight intensity	$I^0(\alpha_s, \beta, Z_s, a)$	[W m <sup>-2</sup> sr <sup>-1</sup> ]		
	Diffuse horizontal irradiance	$D_h(Z_s, a)$	[W m <sup>-2</sup> ]	Eq. (A.2)	Pre-computation of sky and sun coefficients
	Diffuse-to-extra-terrestrial solar horizontal irradiance ratio	$D_h(Z_s, a) / E_{sh,a}(Z_s, a)$	[-]	Typical values <sup>d</sup>	
	Turbidity factor	$T(a)$	[-]	Eq. (A.4)	
	Relative air mass	$m(Z_s)$	[-]		
	Ideal (clean atmosphere) extinction	$\sigma^*(m)$	[-]		
	Sky coefficients	$\Psi_{i,sky}(\alpha_s, \beta, Z_s, a)$	[-]		
	Sun coefficients	$\Psi_{i,sun}(\alpha_s, \beta, Z_s, a)$	[-]	Eq. (12)	
Irradiance ratio scaling	$\xi_{ED}(a)$	[-]	$\sim \mathcal{U}(0.00, 1.25)$ or $\sim \mathcal{U}(0.75, 1.25)^e$	random	
Soot properties	Absorption function of the soot refractive index (@ 531 nm)	$F(m_k)$	[-]	$\sim \mathcal{N}(0.332, 0.0439)$	random
	Scattering-to-absorption function of the soot refractive index (@ 531 nm)	$F(m_k)/F(m_k)$	[-]	$\sim \mathcal{N}(0.901, 0.128)$	
	Soot monomer/primary particle diameter	$d_p$	[nm]	$\sim \mathcal{N}(36, 5.81)$	
	Geometric mean of lognormal aggregate size distribution	$N_g$	[-]	$\sim \mathcal{U}(30, 300)$	
	Geometric standard deviation of lognormal aggregate size distribution	$\sigma_g$	[-]	$\sim \mathcal{N}(2.74, 0.499)$	
	Fractal prefactor (diameter-based)	$k_f$	[-]	$\sim \mathcal{N}(8.145, 0.451)$	
	Fractal (Hausdorff) dimension	$D_f$	[-]	$\sim \mathcal{N}(1.74, 0.0574)$	
	Soot material density	$\rho_s$	[g cm <sup>-3</sup> ]	$\sim \mathcal{N}(1.86, 0.120)$	
	Mass-normalized extinction cross-section	$\sigma_m^*(b)$	[m <sup>2</sup> g <sup>-1</sup> ]	RDG-PFA	Pre-computation of soot/Legendre coefficients
	Single-scatter albedo	$\omega(b)$	[-]		
Scattering phase function	$p(\theta, b)$	[sr <sup>-1</sup> ]			
Soot/Legendre coefficients	$\Phi_l(b)$	[-]	Eq. (10)		
Plume loading	Observed plume transmittance	$\tau_{obs}$	[-]	---	Independent
Camera pointing	Relative solar azimuth	$\alpha_s$	[°]	---	Independent
	Camera inclination	$\beta$	[°]		
	Solar zenith	$Z_s$	[°]		

<sup>a</sup> The means by which variables are randomly drawn or computed.

<sup>b</sup> The method by which a variable is considered in the GUA MC method. Given a set of "independent" and "random" variables, pre-computed data ( $\Psi_{i,sky}(\alpha_s, \beta, Z_s, a)$ ,  $\Psi_{i,sun}(\alpha_s, \beta, Z_s, a)$ ,  $\sigma_m^*(b)$ , and  $\Phi_l(b)$ ) are obtained and used to calculate soot mass column density.

<sup>c</sup> Sky model coefficients are independent variables in the analysis of a single skylight intensity model ( $a \in \{1 \dots 15\}$ ) but, for the derived sky categories ( $a \in \{A \dots D\}$ ), skylight intensity models are randomized following a discrete uniform distribution with support over the skylight intensity models included in the sky category.

<sup>d</sup> Typical values as listed for each CIE sky model as per the literature (Darula and Kittler, 2002; Kittler et al., 2012).

<sup>e</sup> Author-selected distributions:  $\mathcal{U}(0.00, 1.25)$  for CIE sky type 1–6 and  $\mathcal{U}(0.75, 1.25)$  for CIE sky types 7–15.

<sup>f</sup> Prior probability distributions for soot properties were derived by Johnson et al. (2013).

Deleted: MC-...andomized... and pre-computed variables if

Formatted Table

Deleted: MC-...r...andomized

Formatted

Field Code Changed

Deleted: ET

Formatted

Field Code Changed

Formatted

Deleted: (11)(11)(11)

Formatted

Deleted: MC-r...andomized

Deleted:  $E_{(m)}$

Formatted

Deleted:  $b$

Formatted

Deleted: Assorted

Deleted: Fundamental soot properties

Deleted: Ratio of s...cattering-to-absorption functions

Deleted:  $F_{(m)}$

Formatted

Deleted:  $E_{(m)}$

Formatted

Deleted: Fundamental s

Formatted

Deleted: MC-...andomized<sup>f</sup>

Formatted

Deleted: M

Formatted

Deleted:  $\ddagger$

Deleted: (10)(10)(10)

Formatted

Deleted:  $\ddagger$

Formatted

Formatted Table

Deleted: MC-...andomized

Deleted: groups

Deleted: group

Deleted: are listed ...in Table 2 of

**Table 3: Summary of constraints regarding camera pointing relative to the horizon and sun as a function of plume transmittance ( $\tau_{obs}$ ). Compliance with these heuristics ensures that uncertainty in sky-LOSA-computed soot mass column density is low ( $CV_{95} \leq 17\%$ ), regardless of solar zenith angle ( $Z_s$ ). (N.C. = no constraint).**

<u>Sky Category</u>	Camera Inclination Angle, $\beta$	Solar Scattering Angle, $\theta_s$
<b>Plume Transmittance (<math>\tau_{obs}</math>) <math>\leq 0.45</math></b>		
A	N.C.	$\theta_s \geq 13^\circ$
B	N.C.	$\theta_s \geq 23^\circ$
C	$\beta \leq 20^\circ$	$\theta_s \geq 79^\circ$
D	$\beta \leq 25^\circ$	$\theta_s \geq 54^\circ$
<b>Plume Transmittance (<math>\tau_{obs}</math>) <math>\leq 0.70</math></b>		
A	N.C.	$\theta_s \geq 15^\circ$
B	N.C.	$\theta_s \geq 29^\circ$
C	$\beta \leq 16^\circ$	$\theta_s \geq 83^\circ$
D	$\beta \leq 19^\circ$	$\theta_s \geq 59^\circ$
<b>Plume Transmittance (<math>\tau_{obs}</math>) <math>&gt; 0.70</math></b>		
A	$\beta \geq 10^\circ$	$\theta_s \geq 17^\circ$
B	N.C.	$\theta_s \geq 35^\circ$
C	$\beta \leq 13^\circ$	$\theta_s \geq 84^\circ$
D	$\beta \leq 17^\circ$	$\theta_s \geq 62^\circ$

Deleted: Gr

Deleted: oup